Lateral distribution of phosphatidylinositol 4,5-bisphosphate in membranes regulates formin- and ARP2/3-mediated actin nucleation

Received for publication, August 24, 2018, and in revised form, January 13, 2019 Published, Papers in Press, January 28, 2019, DOI 10.1074/jbc.RA118.005552

Robert Bucki[‡§1,2], Yu-Hsiu Wang[¶§§1], Changsong Yang[‖1], Sreeja Kutti Kandy[1], Ololade Fatunmbi[**], Ryan Bradley[**], Katarzyna Pogoda[‡ ‡‡], Tatyana Svitkina[‖], Ravi Radhakrishnan[**], and Paul A. Janmey[‡§§]**

From the Departments of [‡]Physiology, [¶]Chemistry, [‖]Biology, and [**]Chemical and Biomolecular Engineering, University of Pennsylvania, Philadelphia, Pennsylvania 19104, the [§]Department of Microbiological and Nanobiomedical Engineering, Medical University of Białystok, 15-089 Białystok, Poland, the [‡‡]Institute of Nuclear Physics, Polish Academy of Sciences, PL-31342 Kraków, Poland, and the [§§]Institute for Medicine and Engineering, University of Pennsylvania, Philadelphia, Pennsylvania 19104

Edited by Alex Toker

Spatial and temporal control of actin polymerization is fundamental for many cellular processes, including cell migration, division, vesicle trafficking, and response to agonists. Many actin-regulatory proteins interact with phosphatidylinositol 4,5-bisphosphate ($PI(4,5)P_2$) and are either activated or inactivated by local $PI(4,5)P_2$ concentrations that form transiently at the cytoplasmic face of cell membranes. The molecular mechanisms of these interactions and how the dozens of $PI(4,5)P_2$-sensitive actin-binding proteins are selectively recruited to membrane $PI(4,5)P_2$ pools remains undefined. Using a combination of biochemical, imaging, and cell biologic studies, combined with molecular dynamics and analytical theory, we test the hypothesis that the lateral distribution of $PI(4,5)P_2$ within lipid membranes and native plasma membranes alters the capacity of $PI(4,5)P_2$ to nucleate actin assembly in brain and neutrophil extracts and show that activities of formins and the Arp2/3 complex respond to $PI(4,5)P_2$ lateral distribution. Simulations and analytical theory show that cholesterol promotes the cooperative interaction of formins with multiple $PI(4,5)P_2$ headgroups in the membrane to initiate actin nucleation. Masking $PI(4,5)P_2$ with neomycin or disrupting $PI(4,5)P_2$ domains in the plasma membrane by removing cholesterol decreases the ability of these membranes to nucleate actin assembly in cytoplasmic extracts.

Although it constitutes less than 1% of the total phospholipid of the cell, phosphatidylinositol 4,5-bisphosphate ($PI(4,5)P_2$)[3] is implicated in control of many protein functions and, as a result, many different cellular tasks ranging from vesicle trafficking and ion flux at the plasma membrane to chromatin remodeling within the nucleus. One of the earliest and most thoroughly documented effects of this lipid in eukaryotic cells is the control of the actin-based cytoskeleton. Because the same pool of cytoplasmic actin needs to be arranged differently to support the spectrum of its cellular functions, a dynamic lipid-based regulation at the cytoplasm/membrane interface provides a unique mechanism to control and modify actin assembly with spatial and temporal specificity.

Relevance of $PI(4,5)P_2$ to cytoskeletal assembly was first suggested by biochemical studies of its interaction with actin-binding proteins (1), including those that sever actin filaments, nucleate actin assembly, and attach actin filaments to each other and to transmembrane complexes (2). Subsequently, manipulation of enzymes involved in $PI(4,5)P_2$ production showed that increasing cellular $PI(4,5)P_2$ levels massively increased actin assembly (3) and stress fiber formation (4), whereas increasing $PI(4,5)P_2$ degradation globally (5) or locally (6) destabilized actin assembly and actin-dependent processes. Targeted delivery of lipid vesicles containing $PI(4,5)P_2$ or $PI(3,4,5)P_3$ into a *Xenopus* egg extract is sufficient to cause actin assembly at the vesicle that drives its motility through the extract, whereas vesicles with phosphatidylinositol had no effect (7). Similar studies show that filopodial structures form when *Xenopus* extracts are added to supported bilayers containing $PI(4,5)P_2$ (8). Such studies have identified scores of proteins involved in actin remodeling that are affected by $PI(4,5)P_2$ but have not yet led to a clear understanding of how cellular $PI(4,5)P_2$ distribution is controlled in the plasma membrane or how the proteins that are potentially regulated by $PI(4,5)P_2$ compete for this scarce lipid.

The importance of cholesterol in arranging plasma membrane $PI(4,5)P_2$ and the role of $PI(4,5)P_2$ in organizing the cytoskeleton have been previously reported (9). $PI(4,5)P_2$ levels and lateral mobility of plasma membrane proteins are reduced after

This work was supported by National Institutes of Health Grant GM111942 (to P. A. J.) and the National Science Center, Poland, under Grant UMO-2015/17/B/NZ6/03473 (to R. B.). The authors declare that they have no conflicts of interest with the contents of this article. The content is solely the responsibility of the authors and does not necessarily represent the official views of the National Institutes of Health.

This article contains Figs. S1–S9.

[1] These authors contributed equally to this work.

[2] To whom correspondence should be addressed. Tel.: 215-573-9787; Fax: 215-573-6815; E-mail: buckirobert@gmail.com.

[3] The abbreviations used are: $PI(4,5)P_2$, phosphatidylinositol 4,5-bisphosphate; CHOL, cholesterol; dCHOL, dihydrocholesterol; POPC, 1-palmitoyl-2-oleoyl-*sn*-glycero-3-phosphocholine; DOPE, dioleoylphosphatidylethanolamine; DOPS, 1,2-dioleoylphosphatidylserine; NPF, nucleation promoting factor; N-WASP, neural Wiskott-Aldrich syndrome protein; $PI(3,4,5)P_3$, phosphatidylinositol 3,4,5-trisphosphate; LUV, large unilamellar vesicle; VMD, visual molecular dynamics; MβCD, methyl-β-cyclodextrin; L_o, liquid-ordered; L_d, liquid-disordered; GTPγS, guanosine 5′-*O*-(γ-thio)triphosphate; PS, phosphatidylserine; PE, phosphatidylethanolamine; MD, molecular dynamics; mN, millinewton; PIP_2, phosphatidylinositol 4,5-bisphosphate.

This is an Open Access article under the CC BY license.

© 2019 Bucki et al. Published under exclusive license by The American Society for Biochemistry and Molecular Biology, Inc.

cholesterol depletion, suggesting links between PI(4,5)P_2-mediated control of actin assembly (9) and lateral mobility of membrane proteins.

Dozens of actin-binding proteins bind with high specificity to PI(4,5)P_2 (10, 11). In many cases, the domain of the protein responsible for its regulation by the lipid consists largely of multiple basic amino acids interspersed with some hydrophobic residues, rather than a specific folded structure characteristic of a tight binding pocket within a protein for a specific soluble ligand. Measurement of PI(4,5)P_2 diffusion shows that most of the plasma membrane PI(4,5)P_2 pool is bound or sequestered to some extent (12). A major unresolved question is how PI(4,5)P_2 distributes laterally within the plasma membrane and whether all PI(4,5)P_2 molecules are equally effective at binding their targets.

Among other hypotheses for how a relatively scarce small molecule like PI(4,5)P_2 can control the function of hundreds of its target proteins with fidelity is the idea that specific proteins bind PI(4,5)P_2 only when PI(4,5)P_2 is appropriately distributed within the membrane bilayer. For example, *in vitro*, phospholipid vesicles containing PI(4,5)P_2 inhibit the function of the actin-severing protein gelsolin much more strongly when the vesicles undergo a cholesterol-dependent redistribution into liquid-ordered (L_o) and liquid-disordered (L_d) domains (13). Other actin-binding proteins such as N-WASP, talin, and several others bind with different affinities to lipid bilayers containing constant amounts of PI(4,5)P_2 but various amounts of other lipids to which the protein does not bind directly. In a cellular context, the demixing of PI(4,5)P_2 into nanoscale domains that are highly enriched for this minor lipid has been observed using either fluorescent analogs of the lipid or fluorescently labeled lipid-binding proteins, and the targeting of proteins to PI(4,5)P_2 often leads to their distinct localization within the cell. Recent studies show the relevance of nanoscale PI(4,5)P_2 clusters to critical PI(4,5)P_2-triggered cellular functions (14–18). Potential mechanisms that explain how local concentration fluctuations of PI(4,5)P_2 might regulate cellular functions were summarized in a recent review, which combines studies from both experiments and simulations (11).

Here, we test the hypothesis that the lateral distribution of PI(4,5)P_2 within lipid membranes alters its ability to nucleate actin in cell extracts using a combination of purified lipid monolayers, bilayer vesicles, and cell-derived membrane sheets that retain the complexity of the cells' plasma membrane. In all cases, incorporation of PI(4,5)P_2 into these membranes is required for them to nucleate actin assembly. Masking PI(4,5)P_2 within a cell membrane by competitive binding of exogenous ligands or disrupting PI(4,5)P_2 domains within the plasma membrane by removing cholesterol destroys the ability of these membranes to nucleate actin assembly in cell extracts derived from bovine brain and human neutrophils.

Pharmacologic inhibition of the two major actin-nucleating factors, formins and Arp2/3 complex, showed that formins and Arp2/3 were the dominant factors responsible for PI(4,5)P_2-mediated activation of actin assembly in brain and neutrophil extracts. A quantitative analysis of changes in actin assembly caused by increasing concentrations of PI(4,5)P_2, delivered by vesicles of either uniform or demixed composition, showed that the binding kinetics could be best described by a two-state mechanism in which the nucleating factor, presumably a formin, first docks electrostatically to the membrane surface, and then it cooperatively binds three or more PI(4,5)P_2 molecules to acquire actin-nucleating activity. The requirement for simultaneous binding of multiple PI(4,5)P_2 is consistent with a greater effect of PI(4,5)P_2 when it is locally concentrated. The effect of cholesterol (CHOL) on augmenting the effect of PI(4,5)P_2 is supported by a molecular dynamics simulation of the docking of the PI(4,5)P_2-binding site of mDia2 on a lipid bilayer with a variable composition.

Results

Actin assembly on phase-demixed monolayers with Ca^{2+}-induced perturbations

The lateral distribution of actin assembled on a supported lipid monolayer reflects the lateral distribution of PI(4,5)P_2 at the membrane/extract interface as PI(4,5)P_2 serves as a membrane anchor/activator for nucleation-promoting factors such as N-WASP, WAVE2, and formins. The actin assembly assay on supported monolayers therefore provides an imaging-based platform for examining PI(4,5)P_2–protein interactions. To investigate Ca^{2+}-mediated perturbation of PI(4,5)P_2–protein interactions, we adopted an actin assembly assay using supported lipid monolayers. For phase-demixed monolayers that were transferred at 20 mN/m in the absence of Ca^{2+}, the assembled actin filaments were found in both L_o and L_d phases (Fig. 1, *A* and *B*). In contrast, when Ca^{2+} was added to the monolayer prior to its deposition on the glass support, actin filaments were concentrated in one of the phases, namely the L_d phase, as indicated by the partitioning of Rho-DOPE (Fig. 1*C*). The uneven distribution of assembled actin seen by fluorescent phalloidin staining (Fig. 1*D*) and its corresponding quantification showed that the amount of polymerized actin per unit area within the L_o domains was 80% less than that measured in the L_d phase (Fig. 1*E*).

Actin assembly on supported monolayers with Ca^{2+}-induced PI(4,5)P_2 clusters

To further define how actin assembly was affected by the change of the PI(4,5)P_2 lateral structure induced by Ca^{2+}, we examined the efficacy and the localization of actin filament nucleation from cytoplasmic extracts on nondemixed supported monolayers (Fig. 2). For this purpose, lipids from free-standing lipid monolayers formed with or without Ca^{2+} in the subphase were transferred onto coverslips to fix the lipid distribution. The resulting supported monolayers were used for actin assembly and analyzed by both fluorescence and electron microscopy (EM). As revealed by the fluorescence micrographs following phalloidin staining, the densities of actin filaments assembled on supported monolayers transferred in the presence of Ca^{2+} were significantly greater than those transferred in the presence of 5 μM EGTA, although the overall PI(4,5)P_2 mole fraction was the same in both conditions (Fig. 2, *A* and *B*). Brain extracts used in these experiments contained 5 mM EGTA, a large excess over the Ca^{2+} concentration used during lipid transferring, suggesting that it was PI(4,5)P_2 lateral distribution, rather than free Ca^{2+} ions, acting on cytoplasmic pro-

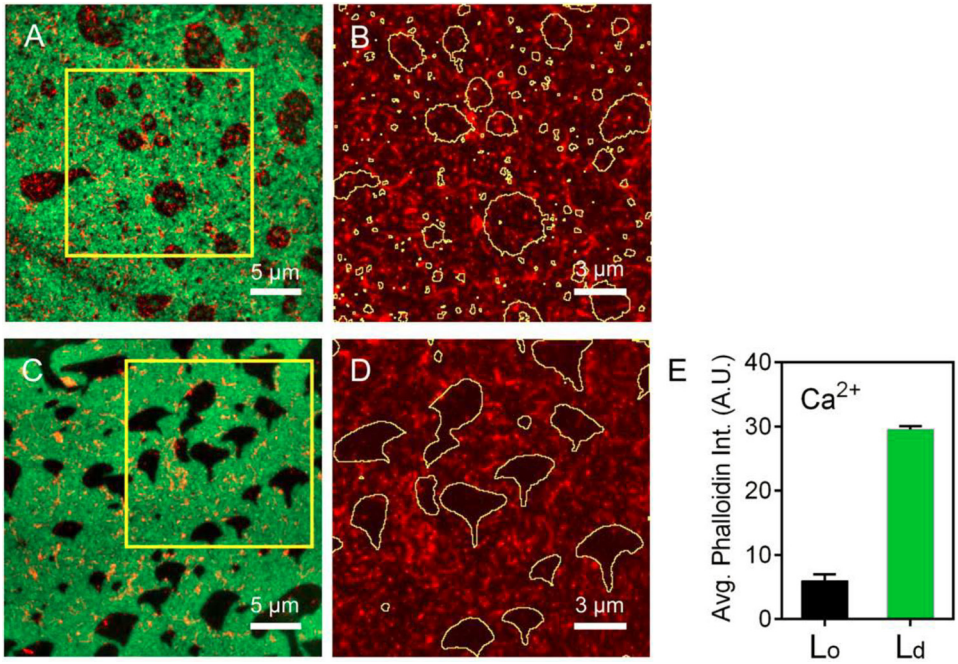

Figure 1. Lateral distribution of actin assembly on supported monolayers at different ionic conditions. *A,* merged fluorescence images of rhodamine-DOPE and Alexa 633-phalloidin–labeled actin filaments on supported monolayers. *B,* lipid microdomain segmentation overlaid with the phalloidin channel at 100 μM EDTA that is enlarged from the *yellow box* marked in *A*. *C,* similar merged micrographs; *D,* enlarged microdomain-segmented micrographs of the Alexa 633-phalloidin channel at 1 mM Ca^{2+}. *E,* quantitative analysis of the mean fluorescence phalloidin intensities within the L_o and L_d phases, respectively, at 1 mM Ca^{2+} (mean ± S.E., $n = 5$ for L_d background; $n = 53$ for L_o microdomains). *a.u.*, arbitrary units.

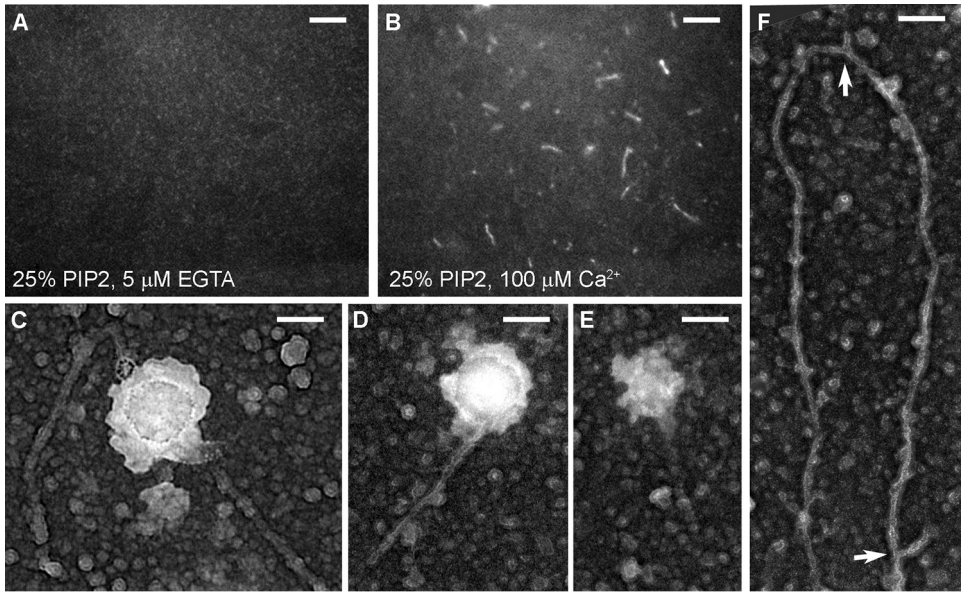

Figure 2. Increased actin assembly induced by PI(4,5)P_2 clusters. *A* and *B,* fluorescence microscopy of phalloidin-stained actin assembly on PI(4,5)P_2/DOPC monolayers without (*A*) and with (*B*) Ca^{2+}. *C–E,* platinum replica EM of PI(4,5)P_2/DOPC monolayers with Ca^{2+} reveals disk-like structures with attached actin filaments. *F,* long actin filaments with occasional branches (*arrows*) are more frequently found on Ca^{2+}-treated supported monolayers. *Scale bars,* 5 μm (*A* and *B*) and 100 nm (*C–F*).

teins that triggered actin polymerization. Further analysis of similar samples by platinum replica EM showed that actin filaments assembled on Ca^{2+}-treated monolayers were attached to round disk-like structures (Fig. 2, *C–E*), which resembled Ca^{2+}-induced nano-sized PI(4,5)P_2 clusters (16). Disk-bound actin filaments were frequently found in Ca^{2+}-treated monolayers but not in Ca^{2+}-free monolayers. These disk-bound actin filaments were mostly long and unbranched. As detected by EM, short branches were found only occasionally (Fig. 2*F*, *arrows*).

Actin assembly induced by PI(4,5)P_2 lipid bilayer vesicles with different lateral structure

We next evaluated actin assembly in cytoplasmic extracts triggered by large unilamellar vesicles (LUVs) that contained PI(4,5)P_2 in the context of mixed or demixed lipid bilayers.

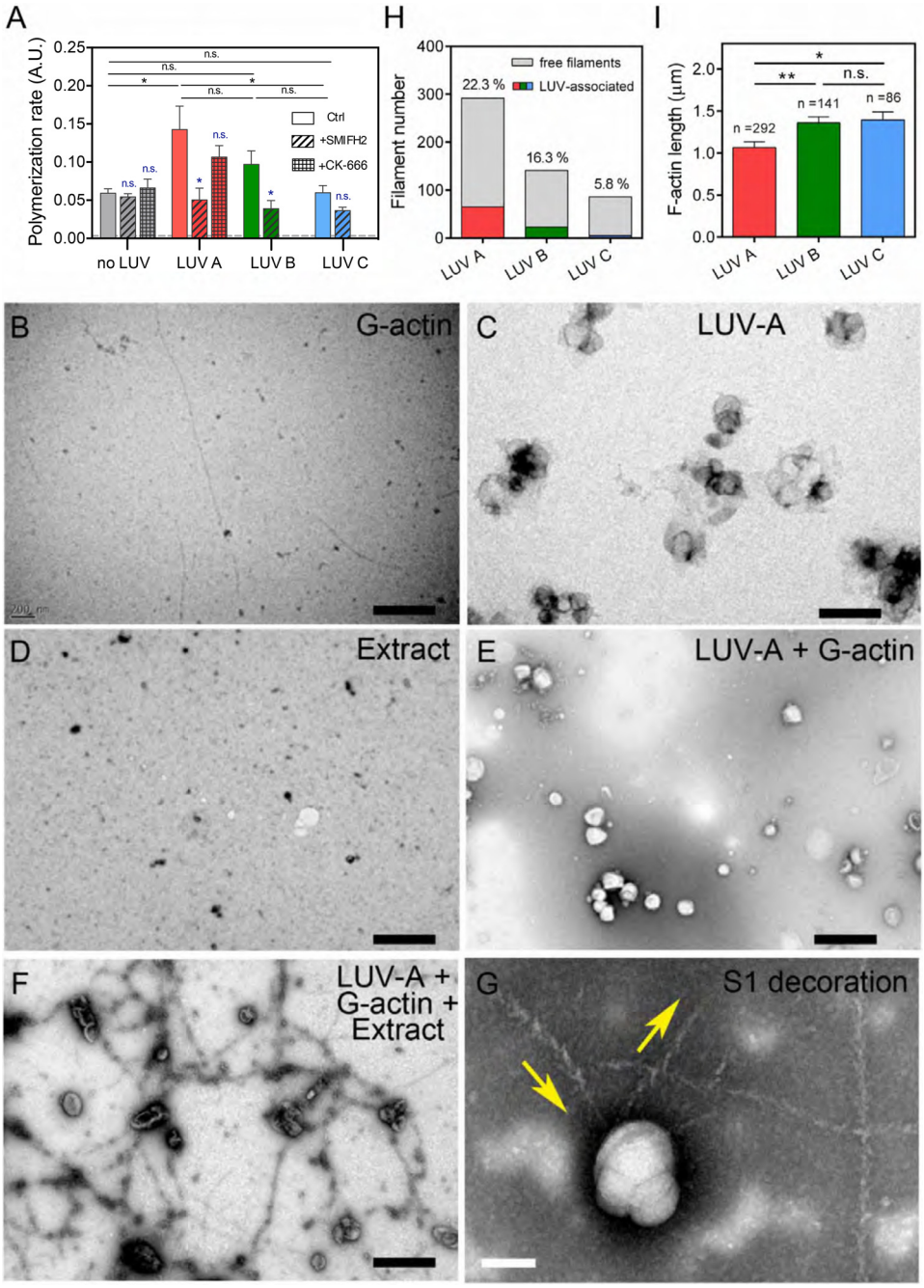

Figure 3. With bilayer vesicles, induction of L_o/L_d phase transition in PI(4,5)P_2-containing vesicles (LUVs A) enables them to nucleate actin assembly in neutrophil extracts better than vesicles (LUVs B) that have the same amount of PI(4,5)P_2 uniformly distributed. *A,* LUVs A-induced nucleation activity is inhibited by a formin inhibitor SMIFH2 (50 μM). Initial rates of pyrenyl-actin polymerization in the presence (+) or absence (−) of neutrophil extracts with or without indicated LUVs. LUVs A: 15% PI(4,5)P_2, 10% DOPC, 30% dCHOL, and 45% DPPC. LUVs B: 15% PI(4,5)P_2 and 85% DOPC; LUVs C: 15% DOPC and 85% DPPC. *B–F,* negative staining EM of structures formed in reaction mixtures containing G-actin only (*B*), LUVs A only (*C*), neutrophil extract only (*D*), G-actin + LUVs A (*E*), neutrophil extract, G-actin, and LUVs A (*F*). *G,* negative staining EM of the same mixture as in *F* after decoration of actin filaments with S1. *Arrows* indicate the direction of pointed ends of actin filaments associated with LUVs A. *H,* total number of free (*gray bars*) or LUVs-associated (*color bars*) actin filaments quantified from EM micrographs of reaction mixtures containing neutrophil extract, G-actin, and indicated LUVs. Percentages of LUV-associated actin filaments are indicated. *I,* average length of actin filaments assembled in the presence of neutrophil extracts containing indicated LUVs quantified from EM micrographs. *A.U.*, arbitrary units; *n.s.*, nonsignificant; *, $p < 0.05$; **, $p < 0.01$. *Scale bars,* 500 nm (*B–E*) and 100 nm (*G*).

Three sets of LUVs prepared by lipid extrusion were tested in this experiment. LUVs A contained 15% PI(4,5)P_2 with 10% DOPC and were phase-demixed by incorporating 30% dihydrocholesterol (dCHOL) in a DPPC background. LUVs B contained the same amount of PI(4,5)P_2 but with a uniform distribution by replacing both dCHOL and DPPC with DOPC (13). LUVs C, which contained no PI(4,5)P_2, served as a negative control and were made out of 15% DOPC and 85% DPPC. The extracts were supplemented with pyrenyl-actin to monitor actin polymerization. When LUVs A or B were added into the cytoplasmic extract, the actin polymerization rate increased significantly by 61 and 20%, respectively, relative to basal actin polymerization rate of the extract alone (Fig. 3*A*). The addition of LUVs C did not promote actin polymerization confirming

the requirement for PI(4,5)P_2 in promoting actin polymerization. The fact that LUVs A were more effective than LUVs B in accelerating actin polymerization suggests that it is not only the global concentration but also the lateral distribution of PI(4,5)P_2 in the membrane that matters for its interaction with cytosolic proteins. We then sought the cytosolic proteins responsible for promoting actin polymerization in the presence of LUVs A and B. The obvious targets were formins and Arp2/3 complex, whose roles in this assay were examined by applying specific inhibitors. SMIFH2 at 50 μM, which inhibits formin-mediated actin assembly (19), greatly suppressed the accelerated actin polymerization mediated by both LUVs A and B. Under the same conditions, the ARP2/3 inhibitor CK-666 (20) at 100 μM did not produce a significant change in the rate of actin polymerization (data not shown). This result suggested that formin-nucleated actin assembly was activated by PI(4,5)P_2 more effectively than nucleation by Arp2/3.

EM analysis of LUV-induced actin filaments

We characterized actin filaments formed in a LUV A-dependent manner by negative staining EM (Fig. 3, *B–I*). The reaction mixture that contained LUVs, actin monomers (G-actin) and the cytoplasmic extract, was applied to EM grids and after a short incubation (1–5 min) prepared for EM (Fig. 3*F*). As a control, we incubated grids with incomplete mixtures containing G-actin only (Fig. 3*B*), LUVs A only (Fig. 3*C*), neutrophil extract only (Fig. 3*D*), or LUVs A and G-actin, but no extract (Fig. 3*E*). G-actin alone or in a mixture with LUVs A produced very few long actin filaments, presumably from spontaneous nucleation, whereas LUVs A alone and extract alone produced no detectable actin filaments. In contrast, when all three ingredients of the reaction were combined, many more actin filaments were observed by EM (Fig. 3*F*). Complete mixtures containing LUVs B or C instead of LUVs A produced significantly fewer but longer actin filaments (Fig. 3, *H* and *I*), suggesting lower frequencies of actin nucleation and a consumption of available monomers by these few nuclei, which led to their more extensive elongation.

Most filaments nucleated in the LUV A-containing reactions were long and unbranched, suggesting a formin-mediated nucleation. We were able to detect only very few reliably identified actin filament branches that might be consistent with nucleation by an Arp2/3-dependent mechanism. Some actin filaments were associated with the vesicles, but many filaments did not contact LUV A vesicles or intersected them, probably because actin filaments were easily released from LUVs after nucleation. We used decoration of actin filaments with myosin subfragment 1 (S1) to determine actin filament polarity relative to LUVs A in EM samples (Fig. 3*G*). These data showed that 64% of the actin filaments attached to LUVs contacted the vesicles by their pointed ends and had their barbed ends oriented away from the vesicle, whereas the remaining 36% had the opposite orientation. These data suggest that after being nucleated at LUVs A, an actin filament is not anchored to the vesicle but elongates freely into the surrounding volume. Because barbed ends grow much faster, the filaments nucleated at the LUVs A on average become oriented with barbed ends away from the vesicle. Despite this fact, a significant fraction of filaments did retain an association of their barbed ends with LUVs A, consistent with formin-mediated nucleation or perhaps capture by a PI(4,5)P_2-activated F-actin–binding protein like α-actinin or talin.

PI(4,5)P_2-dependent actin assembly on plasma membrane sheets

Plasma membranes represent physiologically relevant protein-enriched lipid bilayers at which actin filament polymerization occurs in cells. To evaluate a role of PI(4,5)P_2 in this process, we first developed an actin polymerization assay using isolated plasma membranes from cultured cells. Plasma membranes of attached PtK2 cells expressing membrane-targeted GFP (GFP-C*AAX*, where *AA* is aliphatic amino acid) were isolated by sonication-mediated unroofing. Immunofluorescence staining of PI(4,5)P_2 in these membrane sheets showed numerous bright spots on a background of more uniform staining (Fig. S1*A*). These PI(4,5)P_2 puncta generally did not colocalize with local GFP-C*AAX* enrichments suggesting that they are not membrane folds, but more likely reflect formation of PI(4,5)P_2 clusters in the plasma membrane. Because the anti-PI(4,5)P_2 antibody also recognizes phosphatidylinositol-4-phosphate and PI(3,4,5)P_3, we stained plasma membranes prepared from cells expressing a membrane-targeted catalytic domain of the polyphosphoinositide 5-phosphatase synaptojanin-1 (mRFP-IPP1-C*AAX*) (13). The membranes derived from mRFP-IPP1-C*AAX*–expressing cells showed significantly lower levels of PI(4,5)P_2 immunostaining (Fig. S1). Although synaptojanin-1 can dephosphorylate both PI(4,5)P_2 and PI(3,4,5)P_3, the abundance of PI(3,4,5)P_3 in plasma membranes is much lower than that of PI(4,5)P_2, suggesting that the antibody recognizes PI(4,5)P_2 in the plasma membrane sheets.

Isolated plasma membranes were incubated with brain cytoplasmic extract supplemented with fluorescently labeled G-actin and guanosine 5′-*O*-(γ-thio)triphosphate (GTPγS). Preliminary experiments showed that in contrast to experiments with LUVs in suspension, GTPγS was required to induce robust actin assembly on plasma membrane sheets. In time-course experiments, significant actin assembly occurred after incubation for ~15 min or longer at 37 °C (Fig. S2). Rhodamine-actin assembly in the form of small foci or polymorphic aggregates was clearly detectable by confocal microscopy on GFP-C*AAX*–labeled plasma membranes after 20 min of incubation with the extract (Fig. 4*A*). Immunostaining of PI(4,5)P_2 in these samples revealed some degree of colocalization between the PI(4,5)P_2 signal and sites of actin assembly (Fig. 4*A*, *top*). By plotting the mean fluorescence intensities of PI(4,5)P_2 and rhodamine-actin against each other for individual membrane sheets, we observed a substantial positive correlation between these two values (Fig. 4*B*, *top*).

To evaluate a role of PI(4,5)P_2 in actin assembly on isolated plasma membranes, we incubated membranes with the extract in the presence of neomycin, which binds PI(4,5)P_2 and blocks access of PI(4,5)P_2-interacting partners (21, 22). These experiments showed that neomycin did not significantly decrease the PI(4,5)P_2 immunofluorescence signal (Fig. 4*C*, *left*), presumably being unable to prevent PI(4,5)P_2 interaction with the antibody. However, actin assembly on neomycin-treated plasma mem-

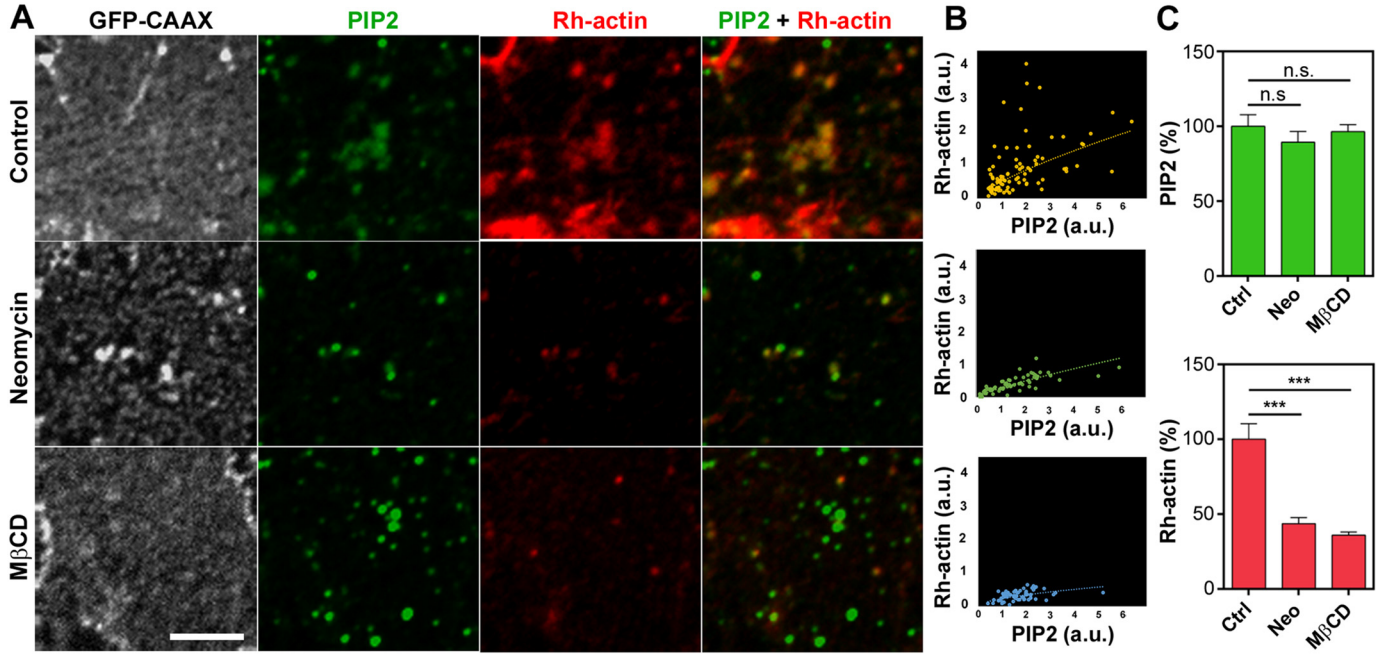

Figure 4. PI(4,5)P_2 is required for actin polymerization on isolated plasma membranes. *A,* fluorescence microscopy of plasma membranes isolated from Ptk2 cells expressing GFP-C*AAX* (*white*) and stained with PI(4,5)P_2 antibody (*green*) after incubation at 37 °C for 20 min with bovine brain extract containing 0.2 μM rhodamine-actin (*red*), ATP, and GTPγS without inhibitors (*top row*), or in the presence of 2 mM neomycin (*middle row*), or 2.5 mM MβCD (*bottom row*). *B,* positive correlation between the mean fluorescence intensities of assembled rhodamine-actin (*y* axis) and PI(4,5)P_2 immunostaining (*x* axis) in individual extract-treated plasma membrane sheets without inhibitors (*top*) or in the presence of neomycin (*middle*) or MβCD (*bottom*); *a.u.*, arbitrary units. *C,* mean fluorescence intensities of PI(4,5)P_2 immunofluorescence (*left*) and assembled rhodamine-actin (*right*) in extract-treated plasma membrane sheets in indicated conditions. *Error bars,* S.E. *Ctrl,* control; *Neo,* neomycin. *N* (regions of interest) = 87 (control), 67 (neomycin), and 67 (MβCD); *n.s.*, nonsignificant; ***, $p < 0.001$. *Scale bar,* 5 μm.

brane sheets was significantly decreased (Fig. 4, *A* and *C*). The remaining low levels of actin assembly still positively correlated with the PI(4,5)P_2 immunoreactivity (Fig. 4*A*).

Cholesterol is important for organizing lipid domains in the plasma membrane and can affect lateral organization of PI(4,5)P_2 within the plasma membrane. To assess a role of cholesterol in lateral organization of PI(4,5)P_2 for actin assembly on plasma membranes, we extracted cholesterol from the membranes by treating membranes with methyl-β-cyclodextrin (MβCD). Staining with filipin (23) confirmed a significant decrease in the cholesterol content in the membrane sheets (Fig. S3). This treatment did not affect the overall immunofluorescence intensity of PI(4,5)P_2 (Fig. 4*C*), and bright PI(4,5)P_2 puncta were still preserved, probably because PI(4,5)P_2 might also be clustered by cholesterol-independent means, for example, within clathrin-coated structures. Importantly, actin assembly on MβCD-treated plasma membranes was significantly reduced (Fig. 4, *A* and *C*) and its levels positively correlated with the PI(4,5)P_2 levels (Fig. 4*B*). These data suggest that membrane structures formed in the presence of cholesterol stimulate actin assembly.

Two major classes of actin nucleators, Arp2/3 complex and formins, are likely candidates to stimulate actin polymerization downstream of PI(4,5)P_2. To determine roles of these nucleators for actin assembly on isolated plasma membranes, we performed the experiments in the presence of an Arp2/3 complex inhibitor CK-666 or a formin inhibitor SMIFH2 (Fig. 5). The results showed that rhodamine-actin incorporation was ~10-fold greater in the presence of the extract than with the buffer alone. The levels of extract-induced actin assembly were reduced by ~80% in the presence of CK-666 and by ~40% in the presence of SMIFH2, indicating that both formins and the Arp2/3 complex contribute to actin assembly on plasma membranes in the presence of the extract supplemented with GTPγS.

Ultrastructure of the PI(4,5)P_2-dependent actin cytoskeleton

We next examined ultrastructural organization of PI(4,5)P_2 and actin filaments using platinum replica EM combined with immunogold labeling of PI(4,5)P_2. Untreated plasma membranes (Fig. 6*A*) were associated with flat or curved clathrin lattices, as commonly observed in unroofed cells (24). However, actin filaments and other cytoskeletal elements were mostly removed in our unroofing conditions. The abundance of PI(4,5)P_2 immunogold labeling was highly variable among cells. However, gold particles typically formed sizable clusters (Fig. 6, *A* and *F*).

When plasma membranes were incubated for 20 min with bovine brain extract, abundant actin filaments were found in association with the membranes by EM (Fig. 6, *B* and *C*). Most actin filaments were relatively long, although branched filaments were also observed. We also noticed significantly more clathrin-coated vesicles and caveolae associated with the membranes after their incubation with the extract, as compared with control membranes. Clusters of PI(4,5)P_2 immunogold in extract-treated samples were often associated with clathrin-coated vesicles (Fig. 6*B*), but even more frequently they colocalized with caveolae (Fig. 6*C*). Importantly, clusters of PI(4,5)P_2 immunogold were observed to associate with actin filaments at the surface of clathrin-coated structures or caveolae. These

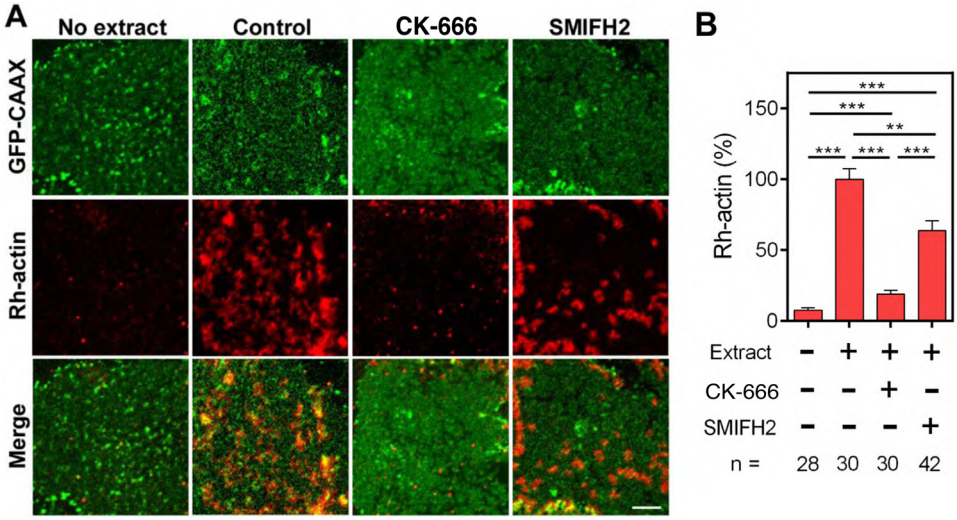

Figure 5. Both Arp2/3 complex and formins are required for actin polymerization on plasma membrane sheets. *A,* fluorescence microscopy of plasma membranes from unroofed Ptk2 cells expressing GFP-C*AAX* (*green*) after incubation at 37 °C for 20 min with solutions containing 0.2 μM rhodamine-actin (*red*), ATP, and GTPγS. Conditions: buffer only (*No extract*); extract only (*Control*); extract containing 50 μM CK-666, and extract containing 100 μM SMIFH2. *B,* mean fluorescence intensities of assembled rhodamine-actin in indicated conditions. *Error bars,* S.E. *n* (regions of interest) are indicated; **, $p < 0.01$; ***, $p < 0.001$. *Scale bar,* 5 μm.

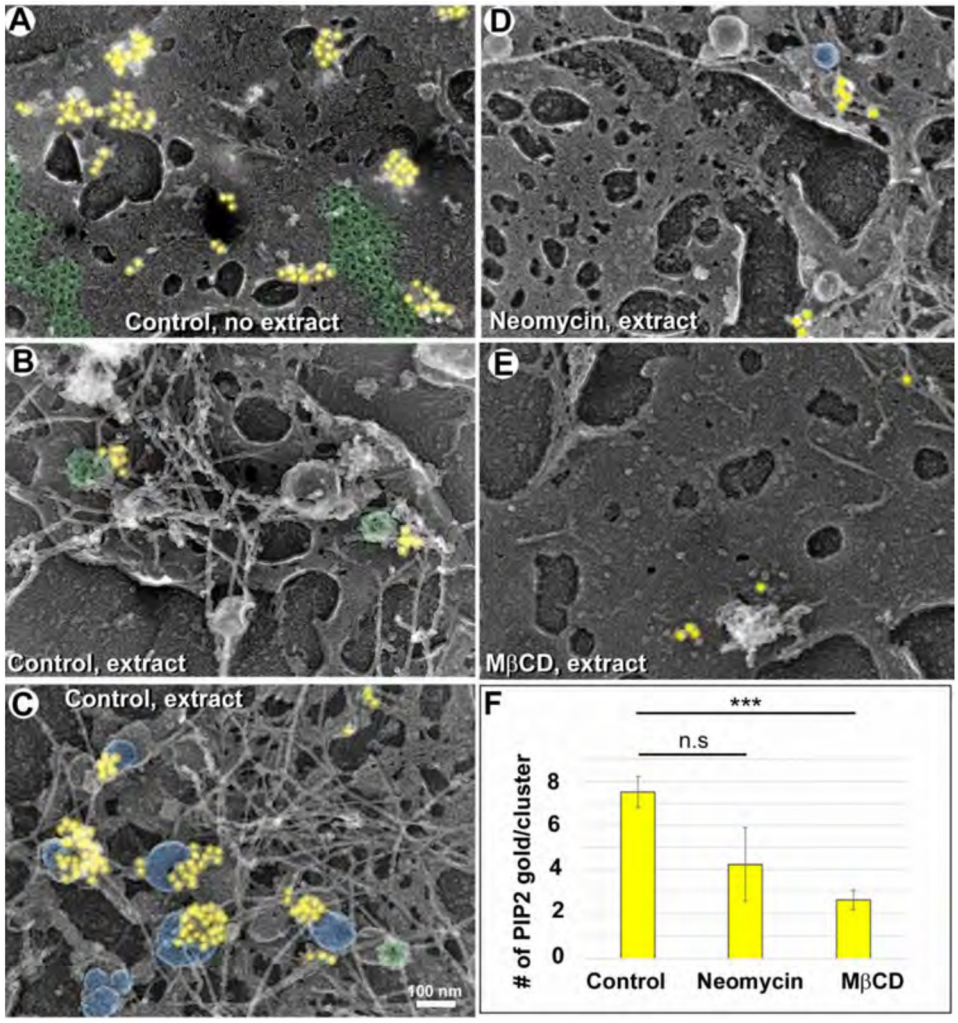

Figure 6. Platinum replica EM of plasma membrane sheets from Ptk2 cells stained with PI(4,5)P_2 antibody (*yellow*). *A,* control plasma membrane sheets lack associated cytoskeleton. *B* and *C,* after incubation with bovine brain extract, sheets are associated with abundant actin filaments, clathrin-coated vesicles (*green*) and caveolae (*blue*). *D* and *E,* plasma membrane sheets incubated with the bovine brain extract containing 2 mM neomycin (*D*) or 2.5 mM MβCD (*E*). *F,* mean number of immunogold particles per cluster in plasma membrane sheets labeled with PI(4,5)P_2 antibody. *Error bars,* S.E. *N* (clusters) = 81 (control), 30 (neomycin), and 27 (MβCD); *n.s.*, nonsignificant; ***, $p < 0.001$.

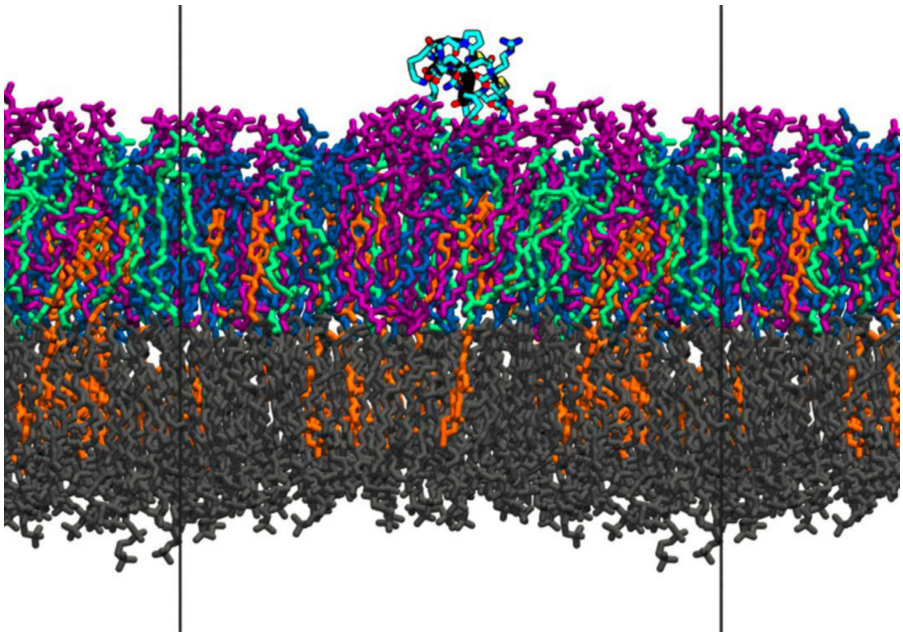

Figure 7. Side view of a typical bilayer containing 20% PI(4,5)P_2 (*purple*), along with PS (*green*), PE (*blue*), CHOL (*orange*), and POPC in the outer leaflet (*gray*). *Vertical bars* indicate the periodic boundaries. The protein, mDia2 (amino acids 25–40), is pictured with atom-colors showing carbon (*cyan*), oxygen (*blue*), nitrogen (*red*), sulfur (*yellow*), and a *black ribbon* indicating the helix. The waters and the ions in the solvent phase are not shown for clarity.

data suggest that the cytoplasmic extract induces assembly of actin filaments, clathrin-coated vesicles, and caveolae on plasma membrane sheets at PI(4,5)P_2-positive sites.

When reactions were performed in the presence of neomycin (Fig. 6*D*) or MβCD (Fig. 6*E*), actin filaments were hardly detectable on the extract-treated plasma membranes by EM. PI(4,5)P_2 immunogold labeling after treatment with neomycin or MβCD was decreased relative to control samples. The results contrast with immunofluorescence data that showed no significant differences in PI(4,5)P_2 signals after treatment with these inhibitors. This discrepancy could be explained by lower accessibility of epitopes for the much larger immunogold-conjugated antibodies, as compared with fluorophore-labeled ones. The PI(4,5)P_2 immunogold in neomycin-treated samples was still clustered with no significant differences in the cluster size, whereas the PI(4,5)P_2 labeling in MβCD-treated samples was usually observed in the form of individual particles or small clusters of 2–3 particles (Fig. 6, *D–F*). This scattered distribution of PI(4,5)P_2 immunogold after treatment with MβCD is consistent with a role of cholesterol in the formation of PI(4,5)P_2-rich domains. Together, these data suggest that *de novo* assembly of actin filaments on plasma membranes in the presence of the cytoplasmic extract depends on the presence of PI(4,5)P_2, as well as on the lateral PI(4,5)P_2 distribution. We also show a connection between PI(4,5)P_2, actin filaments, clathrin, and caveolae.

Cholesterol enhances PI(4,5)P_2-mediated formin activation in a molecular model

To identify the molecular features of enhanced formin binding to vesicles, and to corroborate the mechanism proposed above, we constructed atomistic molecular dynamics (MD) simulations of the protein mDia2 bound to bilayers (see under "Computational methods") containing 20% CHOL in both leaflets, POPC on the outer leaflet and 10, 20, or 30% PI(4,5)P_2 on the inner leaflet along with a PE and PS mixture adjusted to control the surface charge density across conditions. A simulation without cholesterol was performed with 20% PI(4,5)P_2. A typical simulation is depicted in Fig. 7. The number of hydrogen bonds between the protein and the lipids serves as a proxy for binding affinity. We find that the presence of cholesterol enhances binding of mDia2 to PI(4,5)P_2 (Fig. 8). Moreover, the hydrogen bond valence to PI(4,5)P_2 increases with cholesterol, particularly from Arg-25 and Arg-35 (Fig. 9). These residues are incidentally also the most sensitive to the highest PI(4,5)P_2 concentration we studied, suggesting that both cholesterol and increased PI(4,5)P_2 concentration cause the same particular protein bonds to form. Although increased availability of PI(4,5)P_2 may explain the enhanced binding at higher concentrations, the binding enhancement due to cholesterol is observed at a fixed PI(4,5)P_2 concentration. The results of our molecular model support the view that multivalency of the PI(4,5)P_2 recognition peptide binding to the membrane is enhanced by the presence of CHOL at a fixed PI(4,5)P_2 concentration and that the average multivalency is 3–4 under intermediate-to-high PI(4,5)P_2 concentrations of 20–30%.

Quantitative model to describe PI(4,5)P_2-dependent actin filament formation

The symbols in Fig. 10 show the initial actin formation rate as a function of PI(4,5)P_2 concentration for LUVs A and LUVs B added to different extract concentrations. There is a background spontaneous nucleation of actin filaments in the extract. Our model describes the formin-induced nucleation (above and beyond the observed spontaneous nucleation), as described below. For a given number of formin nucleation sites, N_s, the number of actin monomer units incorporated in filaments in the initial time regime is given by Equation 1,

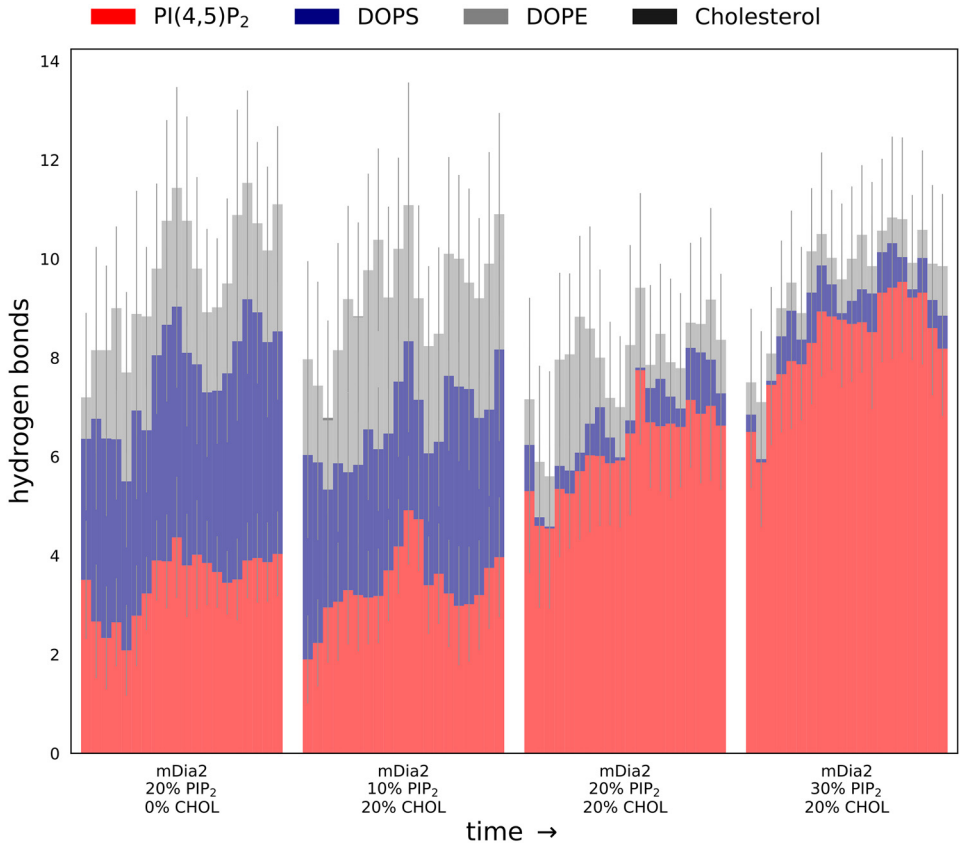

Figure 8. Hydrogen bonds formed between mDia2 and the lipids. *Bars* represent timewise samples of the combined trajectories (two replicates of 150 ns each) for each condition. *Colors* represent lipid types, including PI(4,5)P_2 (*red*), PS (*blue*), and PE (*gray*). Hydrogen bonds with CHOL are rare. CHOL enhances binding of mDia2 to PI(4,5)P_2 at 20% PI(4,5)P_2. As expected, increasing PI(4,5)P_2 concentration also increases protein binding. The compositions are specified in Table 1.

$$n(t) = N_s(k_{on}c_0 - k_{off})t \quad \text{(Eq. 1)}$$

where, k_{on} is the polymerization rate; k_{off} is the de-polymerization rate, and c_0 is the actin monomer concentration. Hence, the initial polymerization rate can be written as shown in Equation 2.

$$P_{rate} = \frac{d}{dt}(N_s(k_{on}c_0 - k_{off})t) \quad \text{(Eq. 2)}$$

Now, assuming that formation of N_s is instantaneous, and k_{off} is negligible, we have Equation 3.

$$P_{rate} = N_s k_{on} c_0 \quad \text{(Eq. 3)}$$

The factor $k_{on}c_0$ is independent of PI(4,5)P_2; hence, the variation of polymerization rate as a function of PI(4,5)P_2 concentration, observed in Fig. 10, can be attributed to the variation of N_s with respect to the PI(4,5)P_2 concentration.

An empirical fit of the actin formation data (shown in Fig. 10) to a Hill curve (shown in Fig. S5) leads to the following observations. (i) All four data sets fit to a Hill coefficient $n \sim 3$, which indicates cooperativity in formin binding to PI(4,5)P_2. (ii) LUVs A have a lower effective K_d (enhanced affinity) compared with LUVs B. (iii) As concentration of extract increases, the effective K_d value decreases for both LUVs A and LUVs B. (iv) Actin formation is observed even in the absence of PI(4,5)P_2, and this depends on the extract concentration.

It is intriguing to note that observations i and ii agree with the molecular dynamics simulations, which suggest an optimal multivalency of 3–4, and where the change in K_d values between LUVs A and LUVs B can be attributed to the enhanced binding in the presence of cholesterol. However, in observation iii, we see a decrease in effective K_d values with an increase in extract concentration that cannot be explained if we assume a single-step binding process of formin to the membrane. Hence, in the following section we present a two-step reaction mechanism that can mimic a change in K_d values as observed; a full description of the development of this model is provided in the supporting information, section S1.

In the proposed two-step reaction, formin (F) first binds to any membrane site (M) as shown in Equation 4,

$$F + M = \rightleftharpoons FM \quad \text{(Eq. 4)}$$

and then the bound formin (FM) can be activated depending on the PI(4,5)P_2 concentration as shown in Equation 5.

$$FM + nP \rightleftharpoons FMP_n \quad \text{(Eq. 5)}$$

Here, P represents PI(4,5)P_2, and n is the Hill coefficient of the reaction. The equilibrium association constants of the first and second reactions are $K_f = ([FM])/([F][M])$ and $K_p = ([FMP_n])/([FM][P]^n)$, respectively. Here, we assume a fraction x

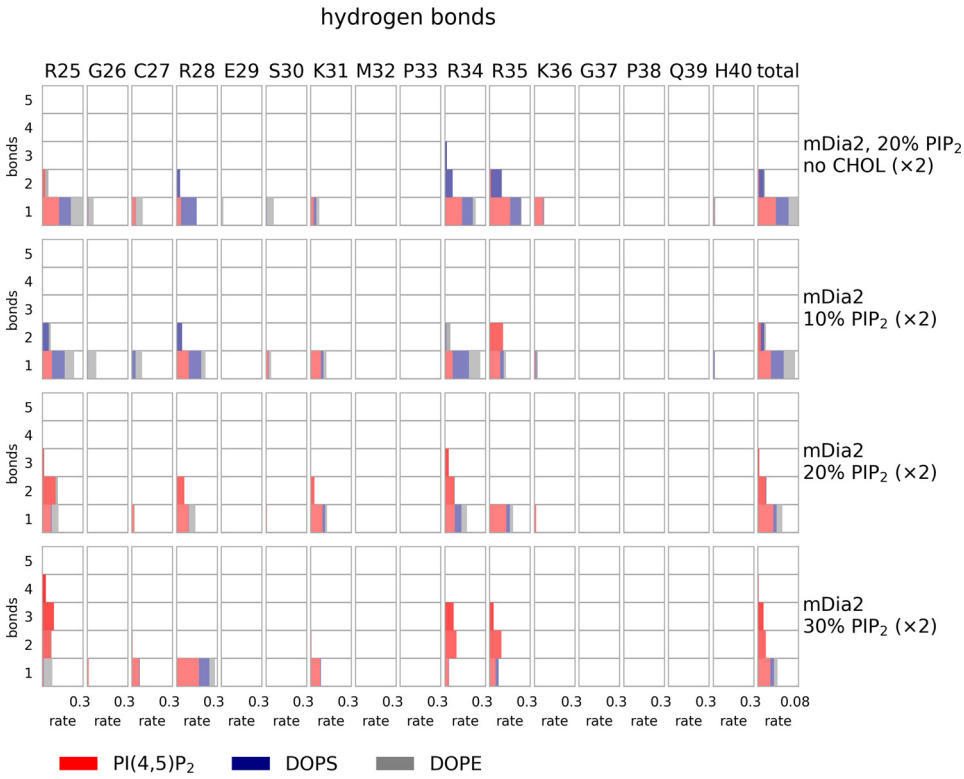

Figure 9. Multivalency distributions for hydrogen bonds formed between mDia2 residues and lipids, colored by type. The multivalency is the number of bonds formed between a protein residue and a single lipid, and the rate is the probability of observing these bonds in a single frame. These histograms are colored for each lipid, including PI(4,5)P_2 (*red*), PS (*blue*), and PE (*gray*). The data are from combined trajectories (two replicates of 150 ns each) for each condition. The multivalent bonds are highly dynamic as indicated by low maximum rates, which nevertheless show a clear preference for PI(4,5)P_2 when it is available at higher concentrations. The total number of hydrogen bonds in the *last column* includes an average of overall bond-forming residues to normalize these data. The *taller, more red* distributions indicate more multivalent PI(4,5)P_2 binding of mDia2 residues. CHOL enhances the selectivity for binding to PI(4,5)P_2 when it is present at 20%. Residues Arg-25 and Arg-34 show the greatest sensitivity to CHOL.

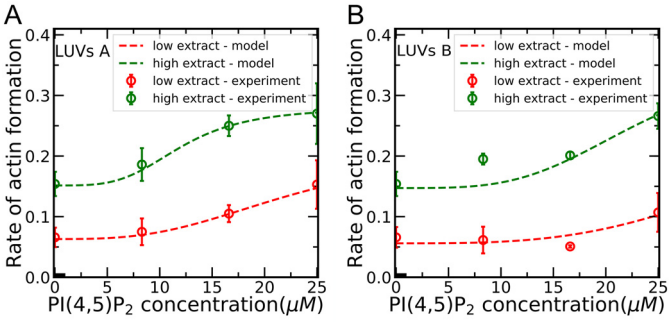

Figure 10. Rate of actin assembly by LUVs A and LUVs B at low (0.5 μM) and high (5 μl) extract concentrations. *Symbols* in the plot correspond to the experimental data for actin polymerization rate as a function of PI(4,5)P_2 concentration. *Dashed lines* correspond to the actin nucleation rate from the proposed reaction mechanisms according to Equations 1 and 9. The parameter values for low and high extract concentrations are as follows: K_p = 0.0001; K_f = 60; [*F*] = 0.1; $[M]_{tot}$ = 0:21, n = 3; and K_p = 0.0001; K_f = 60; [*F*] = 1; $[M]_{tot}$ = 0.28, n = 3.7, respectively.

of *FM* and all of FMP_n can act as nucleation sites for actin. Hence, the concentration of nucleation sites is given by Equation 6.

$$\begin{aligned}[N_s] &= x[FM] + [FMP_n] \\ &= K_f x[F][M] + K_p K_f[F][M][P]^n \\ &= (x + K_p[P]^n)\, K_f[F][M] \end{aligned} \quad \text{(Eq. 6)}$$

Because the total membrane sites $[M]_{tot}$ can be written as shown in Equation 7,

$$[M]_{tot} = [M] + [FM] + [FMP_n] = [M](1 + K_f[F] + K_p K_f[F][P]^n) \quad \text{(Eq. 7)}$$

we can rewrite $[M]$ in terms of total membrane sites as shown in Equation 8.

$$[M] = \frac{[M]_{tot}}{(1 + K_f[F] + K_p K_f[F][P]^n)} \quad \text{(Eq. 8)}$$

Hence, the concentration of nucleation sites is given by Equation 9.

$$[N_s] = \frac{(x + K_p[P]^n)\, K_f[F][M]_{tot}}{(1 + K_f[F] + K_f K_p[F][P]^n)} \quad \text{(Eq. 9)}$$

A comparison of actin formation rate in the proposed reaction with the experimental data is shown in Fig. 10. This mechanism captures all four of the observations obtained from the experiments.

Model to describe actin filament length distribution

As described in Equation 9 and depicted in Fig. 10, the number of actin nucleation sites on the membrane depends on PI(4,5)P_2 and cholesterol concentration. To obtain the length distribution of actin filaments as a function of the number of

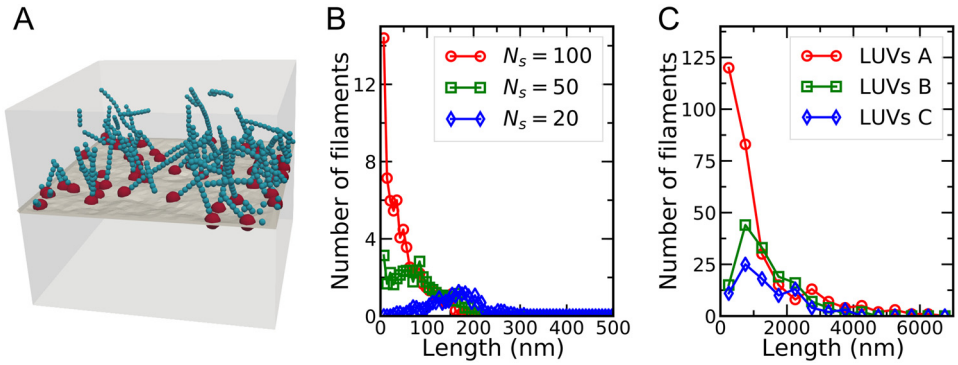

Figure 11. *A,* snapshot of the actin-membrane simulation. *Red beads* represent nucleation sites and *blue* the actin filaments. Free monomers of actin are not shown. *B,* length distribution of actin filaments when the number of nucleation sites are N_s = 20, 50, and 100. *C,* length distribution of actin filaments from experiments with LUVs A, LUVs B, and LUVs C.

nucleation sites, we utilized a spatial model for describing actin-filament formation on the membrane, as described under "Computational methods." In this model, actin monomers can polymerize at the nucleation sites on the membrane surface. A snapshot of the simulation is shown in Fig. 11*A*. Length distributions of actin filaments for different concentrations of nucleation sites obtained from simulations are shown in Fig. 11*B*. Our results are in striking agreement with the experimental observations of the length distributions upon adding the different LUVs as determined from EM studies, see Fig. 11*C*. The length distributions of actin filaments in LUVs A, LUVs B, and LUVs C show LUVs A having a large number of short filaments and LUVs C with the least. The observed trends in the length distributions of actin filaments are consistent with the expectation of exponential distribution at equilibrium (long times) and peaked distributions at intermediate times.

Discussion

Role of cholesterol in PI(4,5)P_2-containing monolayers

Actin assembly on supported monolayers allows a direct observation of the spatial correlation between PI(4,5)P_2-regulated actin–binding proteins and PI(4,5)P_2 nanoclusters. PI(4,5)P_2 serves as a membrane anchor/activator for actin nucleation–promoting factors such as N-WASP (25) and WAVE2 (26) and the formins mDia1 and mDia2 (27, 28). The distribution of actin assembled on a supported lipid monolayer reflects the lateral distribution of the membrane lipids capable of activating actin nucleators. Such a functional assay is independent of fluorescent PI(4,5)P_2 analogs and therefore free from potential artifacts arising from modifying the physical chemistry of the phospholipid. To perturb PI(4,5)P_2 distribution in the membrane, we introduced two elements in our experimental settings. The first component is dCHOL, which was used instead of CHOL to avoid photooxidation. The incorporation of dCHOL, similar to that of CHOL, promotes the lipid-phase separation in both monolayer and bilayer membranes, although with a slightly different phase behavior (29). In a typical ternary phase diagram for bilayer membranes composed of CHOL, saturated and unsaturated lipids such as DPPC and DOPC, the tie-line suggests that the mole fraction of unsaturated lipids can reach 70–75 mol % in the L_d phase, but it is only 10–15 mol % in the L_o phase upon demixing (30). Because the naturally occurring brain PI(4,5)P_2 species 1-stearyl-2-arachidonyl-PI(4,5)P_2 and dioleoyl-PI(4,5)P_2 (31) used here both have unsaturated acyl chains, their distribution is similar to that of the unsaturated DOPC used in our monolayers. These compositions predict a nearly 3-fold increase of the PI(4,5)P_2 surface charge density in the L_d phase upon phase demixing when the total mole fraction of unsaturated lipids in LUVs A was controlled at 25 mol % experimentally. The resulting increase in the local charge density as well as the surface potential leads to an enhanced electrostatic interaction (32). Such an effect of PI(4,5)P_2 lateral segregation was demonstrated to be very effective in mediating gelsolin activity *in vitro* (13).

Role of calcium

Another important factor is Ca^{2+}-induced perturbation of PI(4,5)P_2 lateral distribution (33). The formation of PI(4,5)P_2 nanoclusters induced by Ca^{2+} has two consequences: 1) increased chemical potential of PI(4,5)P_2 within the cluster, and 2) the silencing effect of Ca^{2+} due to charge neutralization. Depending on the interaction with PI(4,5)P_2, whether it is a receptor–ligand type of interaction such as a PLCδPH domain or a pure electrostatic interaction such as MARCKS peptide, the net effect of Ca^{2+} for a PI(4,5)P_2–protein interaction might be different. The former has been investigated recently in both *in vitro* (34) and in cellular studies (18) in which the recognition of PI(4,5)P_2 by PLCδPH domain was suppressed by Ca^{2+} through forming Ca^{2+}–PI(4,5)P_2 complexes. The latter case was investigated in this study by an actin assembly assay sensitive to actin nucleation-promoting factors that interact with PI(4,5)P_2 through an unstructured polybasic motif. The effect of Ca^{2+} and CHOL are not mutually exclusive, and we therefore also considered scenarios where both were present in the system.

Effect of PI(4,5)P_2 clustering

Starting with supported lipid monolayers, we noticed that dCHOL-mediated phase demixing and changes in PI(4,5)P_2 lateral distribution affected actin assembly only when there was Ca^{2+}. The assembled actin filaments distributed evenly among L_o and L_d phases in the absence of Ca^{2+} and associated primarily with the L_d phase when there was Ca^{2+}. The fact that actin assembly was excluded from the L_o microdomain in the pres-

ence of Ca^{2+} leads to two possible explanations: 1) PI(4,5)P_2 is either excluded from the L_o phase in the presence of Ca^{2+} or 2) PI(4,5)P_2 in the L_o domain is "silenced" upon Ca^{2+} adsorption. Because the brain extract contains 5 mM EGTA, trace amounts of Ca^{2+} carried over from lipid transferring were removed by EGTA. The differences in the assembled actin distribution could then only result from Ca^{2+}-induced perturbation in PI(4,5)P_2 lateral distribution, as the "silencing" effect mediated by the formation of Ca^{2+}–PI(4,5)P_2 complexes should be eliminated by EGTA. Although EM provides no direct evidence that these round disk-like structures are PI(4,5)P_2-enriched clusters, the sizes of such structures (~70–120 nm in diameter as shown in Fig. 2, *C–E*) fall within the same size distribution of Ca^{2+}-induced PI(4,5)P_2 clusters under the same conditions (84 ± 24 nm in diameter) that were measured by atomic force microscopy (33, 35).

Effect of PI(4,5)P_2 local concentration and spatial organization in bilayer vesicles

In the experimental system employing LUVs, in which lateral mobility of lipids is not restricted by adsorption to glass, the presence of cholesterol efficiently enhanced the ability of PI(4,5)P_2 to stimulate actin polymerization in the presence of cytoplasmic extracts. Because the amount of PI(4,5)P_2 was the same in cholesterol-containing LUVs A and in cholesterol-lacking LUVs B, these results suggest that lateral demixing of PI(4,5)P_2 induced by cholesterol is responsible for the increased PI(4,5)P_2 ability to stimulate actin assembly.

Role of actin nucleation factors

The increased actin polymerization in extracts containing LUVs A can be explained by additional nucleation and/or enhanced elongation of actin filaments. Because our extracts exhibited basal levels of actin polymerization even in the absence of LUVs, we cannot strictly distinguish between these possibilities. However, using specific inhibitors of the Arp2/3 complex and formins we found that LUV A–mediated enhancement of actin assembly largely depends on formins, but not significantly on the Arp2/3 complex. Similar conclusions can be derived from our EM data that show predominantly unbranched actin filaments in LUV A-containing reaction mixtures. An apparent conflict with other studies that reported a role of Arp2/3 complex in PI(4,5)P_2-dependent actin assembly in cytoplasmic extracts (7, 8) can be explained by the fact that in contrast to other studies, we did not add GTPγS to the reaction mixture in these experiments. GTPγS helps to maintain Rho family GTPases in the extract in an active state. In turn, active Cdc42 and Rac GTPases are necessary to activate nucleation-promoting factors N-WASP and WAVE complex, respectively, for stimulation of Arp2/3 complex activity. Our results obtained with the Arp2/3 complex inhibitor are therefore consistent with this notion.

Effect of formins

The role of formins in this assay can include both nucleation and elongation of actin filaments. Interestingly, although activation of formins also depends on Rho GTPases (36), our experiments suggest that formins can be activated in the absence of a GTPγS-mediated boost of Rho GTPase activity, if LUVs A with demixed PI(4,5)P_2 are provided. The formins mDia1 (27) and mDia2 (28, 37) can interact with acidic phospholipids through their N-terminal basic domains. This interaction contributes to proper localization of these formins in cells (27, 29). Our data suggest that phospholipids contribute not only to localization of formins, but also to their activation. It is likely that in normal endogenous conditions in cells Rho GTPases and phospholipids cooperate for activation of formins.

In cells, polymerizing barbed ends of actin filaments are typically oriented toward and anchored to the plasma membrane by barbed end-associated proteins, such as formins and Ena/VASP family proteins. The proteins of both families directly interact with the barbed ends, whereas their association with the plasma membrane partially or completely depends on other membrane-anchored proteins. This property of the plasma membrane apparently is not reproduced in the mixture of LUVs and the cytoplasmic extract, which can explain the frequent release of actin filaments from LUVs A observed in our experimental system.

Cell-derived plasma membrane sheets as PI(4,5)P_2-dependent actin-nucleating surfaces

As a more physiological assay to test the role of PI(4,5)P_2 in actin assembly, we used isolated plasma membrane sheets as a lipid interface, which we exposed to cytoplasmic extracts. In these assays, we supplemented the cytoplasmic extracts with GTPγS, because we were not able to obtain robust actin assembly on the plasma membrane in the absence of GTPγS. Accordingly, we found that both the Arp2/3 complex and formins contributed to actin assembly in these conditions. Quantitative data suggest some cooperation between the two assembly mechanisms, because the effects of the two inhibitors were not simply additive. We envision two nonexclusive ways of cooperation between formin and Arp2/3-dependent polymerization. Formins might nucleate initial "mother" filaments to enable subsequent Arp2/3 complex– dependent branched nucleation. In contrast, formins may capture barbed ends of Arp2/3 complex–nucleated actin filaments and promote their elongation. Our EM data showing predominantly long actin filaments with infrequent branches are more consistent with the latter scenario.

Our evaluation of the roles of PI(4,5)P_2 for actin assembly on plasma membranes included two complementary assays. Using neomycin, we tested a role of PI(4,5)P_2 availability to proteins in the extract. Using MβCD, we tested whether the lateral organization of PI(4,5)P_2 in the plasma membrane is important. Our data show that both availability and distribution of PI(4,5)P_2 in the plasma membrane are important for actin assembly. This conclusion is further validated by strong positive correlation between the degree of actin assembly and the presence of PI(4,5)P_2 in individual membrane sheets, both in control samples and samples treated with the inhibitors, in which the overall levels of actin polymerization were significantly diminished by neomycin or MβCD treatment. Moreover, the availability and distribution of PI(4,5)P_2 were similarly important for the assembly of other membrane-associated structures, clathrin-coated pits and caveolae, suggesting that our findings may be

applicable to a much broader range of PI(4,5)P_2-interacting proteins.

Molecular model of formin-membrane binding

We constructed a molecular model of a peptide derived from the mDia2 basic domain interacting with bilayers of different compositions and conducted molecular dynamics simulations to infer the molecular interactions, mechanisms, and dynamics of formin recruitment to the membrane and the role of cholesterol in mediating the interactions. At the atomic scale, we designed computational models of peptide–bilayer interactions with and without cholesterol and at varying concentrations of PI(4,5)P_2. We performed all-atom MD simulations for 150 ns to study the interactions. Through these studies, we could validate the hypothesis that interaction between the basic domain peptide of mDia2 and PI(4,5)P_2, as tracked by the temporal evolution of hydrogen bonds between peptide residues and lipid headgroups, is highly dependent on bilayer composition, and specifically the concentration of PI(4,5)P_2. Interestingly, we found that cholesterol plays a significant role in defining the multivalency of the cooperative PI(4,5)P_2–peptide-binding interactions, with a characteristic Hill coefficient between 3 and 4. The experimental results for polymerization rate show cooperativity in formin binding to PI(4,5)P_2 with a Hill coefficient of 3, consistent with the finding of molecular dynamics simulations.

Kinetic model of PI(4,5)P_2-stimulated actin assembly

Complementing the molecular models, we described the kinetics of actin filament formation using kinetic models defining the peptide protein cooperative interactions as well as spatial models of actin polymerization on the membrane. These models describe the interactions at the microscale, in which the formin–PI(4,5)P_2 interactions and the effect of cholesterol were considered through the binding constants. We showed that the effect of PI(4,5)P_2 concentration, cholesterol, and extract concentration are simultaneously captured by a single unified model whose parameters are consistent with the findings of the molecular dynamics simulations. The salient findings include the following. (*a*) The presence of cholesterol enhances formin binding to PI(4,5)P_2 resulting in lower effective K_d values for LUVs A compared with LUVs B; this lowering of the effective K_d is consistent with the enhancement in multivalent interactions observed in the molecular dynamics simulations when cholesterol was included in the bilayers. (*b*) The change in K_d with increase in formin, PI(4,5)P_2, and cholesterol concentration can be explained by a two-step reaction mechanism of formin recruitment to the membrane and multivalent binding with PI(4,5)P_2; moreover, the parameters of the kinetic model are consistent with the findings of molecular simulations. (*c*) Our results suggest that as formin (extract) concentration increases, the number of filament nucleation sites N_s can saturate at a lower concentration of PI(4,5)P_2. This behavior mimics a change in K_d values as seen in the experimental data. This model enables us to simultaneously describe the filament formation rates *versus* PI(4,5)P_2 concentration under low and high extract concentrations with a single (unified) set of parameters. (*d*) The spatial model of actin polymerization successfully explains the experimentally observed length distribution of actin filaments for the different LUVs.

Interpretation of molecular dynamics and modeling

Although the agreement of the molecular model and the kinetic model with the reported experiments is intriguing, it raises the important question as to the mechanism behind cholesterol-mediated enhancement of binding of the peptide to the bilayer. In Fig. 12, we show four snapshots of lipid clustering at the site of the peptide (different rows) from our molecular dynamics simulations for systems without cholesterol (*1st* and *2nd columns*) and with CHOL (*3rd* and *4th columns*). The snapshots indicate that in the presence of cholesterol, there is more PI(4,5)P_2 being recruited, which is consistent with the enhancement in multivalent interactions as reported in Fig. 9. We reiterate that the interactions are primarily electrostatic involving the charged residues of the peptide as noted earlier; this finding is also consistent with protein–lipid interactions observed in molecular dynamics simulations of other related systems reported recently (37, 38). However, the altered presentation of PI(4,5)P_2 to the peptide mediated by the presence of cholesterol does not have an electrostatic origin because there is no significant hydrogen bonding between cholesterol and PI(4,5)P_2 or PS (Fig. S4). Instead, the excluded volume and van der Waals interactions between the CHOL and the acyl chains of the lipids (*i.e.* lipid without the headgroup) are responsible for the CHOL-mediated interactions. In support of this claim, we report the radial distribution functions between lipids (Fig. 13). We find that in general CHOL reduces lipid–lipid distances slightly (see Fig. 13, *upper left*). Ordering between PS and PI(4,5)P_2 disappears above 10%, and both CHOL and high PI(4,5)P_2 concentrations cause higher PS–PS ordering. The high PI(4,5)P_2 concentration shows the most ordering between CHOL and PS. These observations lead us to conclude that there is enhanced CHOL–PS and PS–PS structuring at the nearest neighbor level, and this CHOL-mediated reconfiguration facilitates a better presentation of the PI(4,5)P_2 local cluster to interact with the peptide as observed in the snapshots of Fig. 12. We hypothesize that compositions that encourage formin–PI(4,5)P_2 binding also result in PI(4,5)P_2–PS repulsion. Analysis of lipid–lipid hydrogen bonding and salt bridges (Fig. S4) shows that the reordering observed in the radial distribution functions is not visible in the inter-lipid bonding, which appears to be mostly opportunistic. An abstract measurement of lipid-binding partners (Fig. S4) shows that most lipids have no significant preference for particular lipid neighbors. This suggests that cholesterol and PI(4,5)P_2 concentration effects observed here are not due to lateral rearrangements of these lipids but to subtle differences in both packing and the particular molecular conformations of the PI(4,5)P_2.

Conclusion

A combination of biochemical and computational studies shows that the lateral distribution of PI(4,5)P_2 within the lipid bilayer of the plasma membrane is an essential element in the control of actin assembly at the cell cortex. PI(4,5)P_2-dependent nucleation of actin polymerization involves the function of both formin and nucleation-promoting factors that activate the

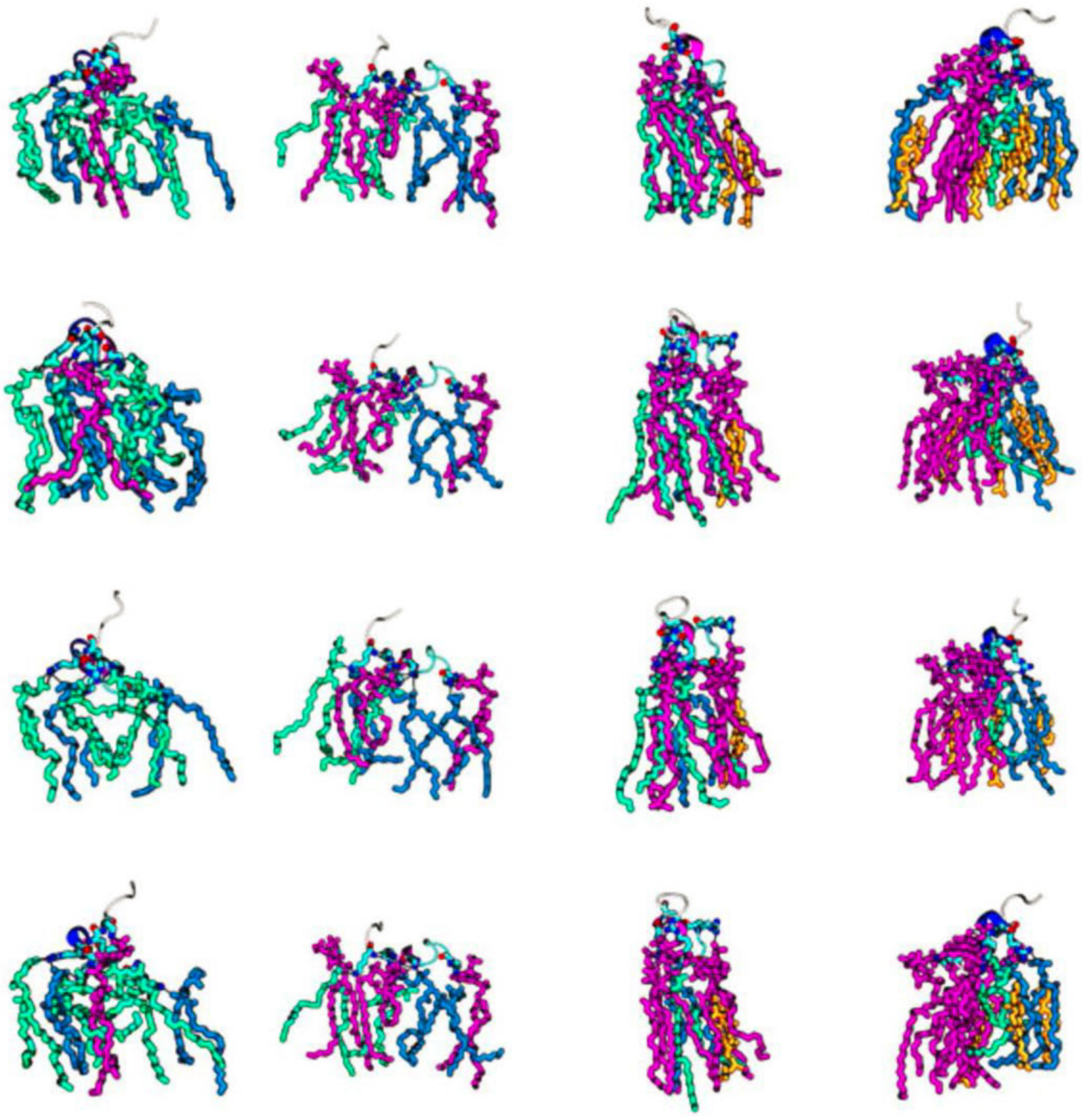

Figure 12. Four representative snapshots (*rows*) for each condition that highlights lipids forming hydrogen bonds with the peptide without CHOL (*1st* and *2nd columns*) and with CHOL (*3rd* and *4th columns*) at the same PI(4,5)P_2 concentration of 20%. The color scheme is the same as in Fig. 7: PI(4,5)P_2 (*purple*), along with PS (*green*), PE (*blue*), CHOL (*orange*), and POPC (*gray*).

ARP2/3 complex. The latter activity also requires GTP. The greater activity of PI(4,5)P_2 to stimulate formin-dependent activation when the lipid is in a phase-separated membrane is consistent with molecular dynamics simulations and analytical models supporting a mechanism in which formin first binds in an inactive state to the membrane and then cooperatively binds 3 eq of PI(4,5)P_2 to initiate actin nucleation. The computational models we have presented at the molecular and microscales collectively provide an integrated framework for the mechanism of actin filament formation induced by nucleating factors such as formin and quantitatively define the roles played by the lipid composition, namely PI(4,5)P_2 and cholesterol, on the filament formation rates.

Experimental procedures

Preparation of supported lipid monolayers

Synthetic PI(4,5)P_2 with uniform acyl chain (1,2-dioleoyl-*sn*-glycero-3-phosphatidylinositol 4,5-bisphosphate), other neutral phospholipids, such as 1,2-dioleoyl-*sn*-glycero-3-phosphocholine (DOPC), 1,2-dipalmitoyl-*sn*-glycero-3-phosphocholine (DPPC), and fluorescently labeled L_d marker,

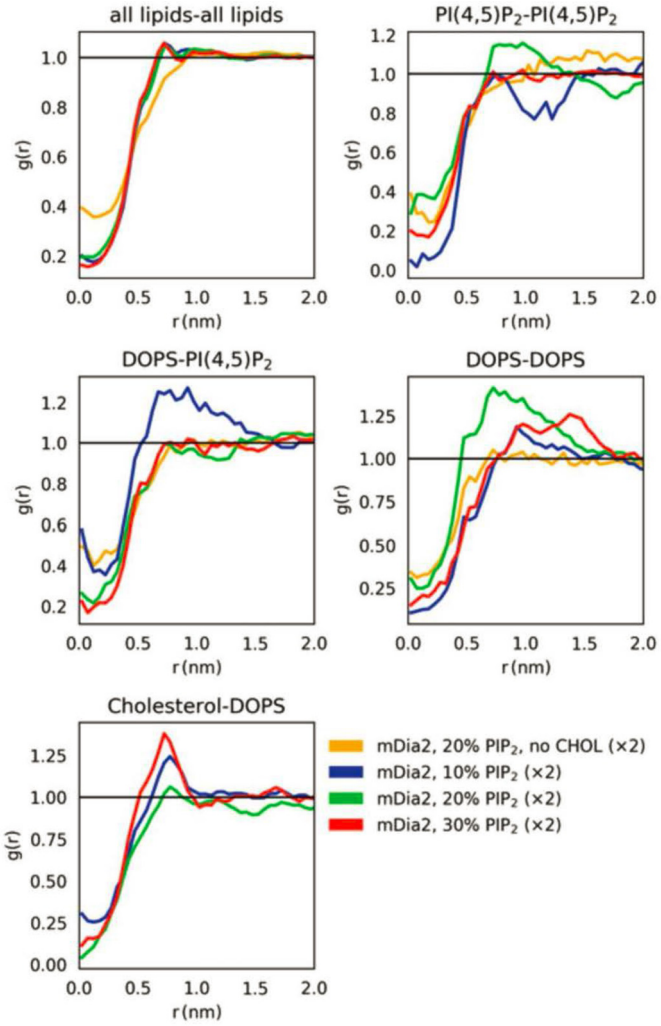

Figure 13. Radial distribution functions between lipids for each simulation condition. In the calculations of these functions, the headgroups of the lipids were not included; in this respect, these represent headless radial distribution functions. All lipids are less ordered when cholesterol is absent (*yellow curve, upper left*) according to the lower peak shifted to slightly higher distances. At low PI(4,5)P_2 concentration, PS associates more with PI(4,5)P_2 (*blue curve*). High 30% PI(4,5)P_2 concentration (*red*) also increases lateral association of CHOL and PS. This result suggests that increasing PI(4,5)P_2 concentration repels PS and causes it to more closely interact with both CHOL (if present) and other PS molecules.

1,2-dioleoyl-*sn*-glycero-3-phosphoethanolamine-*N*-(lissamine rhodamine B sulfonyl) (rhodamine-DOPE) were from Avanti (Alabaster, AL). Dihydrocholesterol (dCHOL, also known as cholestanol) was purchased from Sigma. Subphase reagents HEPES, EDTA, $CaCl_2$, $MgCl_2$, NaCl, and KCl were purchased from ThermoFisher Scientific (Hampton, NH). Dithiothreitol (DTT) was purchased from Research Product Int. Corp. (Mt. Prospect, IL).

Free-standing lipid monolayers were first prepared on a MicroTroughX (Kibron Inc., Helsinki, Finland), which was controlled by the FilmWare 3.57 software package (Kibron Inc.). Pre-mixed lipid solutions doped with rhodamine-DOPE were deposited on a buffered subphase (10 mM HEPES, 150 mM KCl, 100 mM EDTA, 5 mM DTT) at the air/water interface. Lipid monolayers were either transferred onto clean coverslips as such or after 1 mM Ca^{2+} was added, using the Langmuir-Schaefer method. Lipids were transferred onto the coverslips at 20 mN/m surface pressure, corresponding to an initial area per lipid of around 90 $Å^2$, using the motor module (Kibron Inc.). Depending on the purpose, the supported lipid monolayers were either blown-dried to remove residual and stored at room temperature for imaging studies or were stored in PBS to be used in actin assembly assay. For imaging studies, air-dried supported lipid monolayers could be stored at room temperature up to several days without significant changes in their lateral structures; for actin assembly studies, supported lipid monolayers in PBS were to be used within 1–2 days.

LUVs preparation

LUVs bilayers containing PI(4,5)P_2 that demix to different extents (LUVs A) and in fully mixed bilayers (LUVs B) were prepared based on a known phase diagram for a ternary lipid mixture containing DOPC/DPPC/dCHOL (30). Here, dCHOL was used instead of conventional cholesterol to prevent potential artifacts that could result from the photooxidation of the conventional cholesterol. Briefly, to prepare PI(4,5)P_2-containing LUVs A (PI(4,5)P_2, 15%; DOPC, 10%; dCHOL, 30%; DPPC, 45%) and LUVs B (PI(4,5)P_2, 15% and DOPC, 85%), each containing 86 μg of PI(4,5)P_2 was mixed with lipids at a desired composition in chloroform in a glass test tube and blown-dried under nitrogen. Traces of organic solvent were removed by vacuum drying for at least 3 h. Subsequently, the dried lipid film was rehydrated with 200 μl of buffer containing 2 mM Tris, 0.5 mM DTT, 150 mM KCl, pH 7.0. The rehydrated lipid film was then sonicated in a water bath sonicator for 10 min and extruded through a polycarbonate membrane with an average pore size of 200 nm (Avestin, Ottawa, CA) using a mini-extruder (Avanti, Alabaster, AL) on a hot plate at 60 °C. The lipid resuspension was extruded 31 times to ensure proper mixing. The effective PI(4,5)P_2 concentration for LUVs A and B stock solutions was ~250 μM, which considers only the PI(4,5)P_2 in the outer leaflet assuming equal distribution of PI(4,5)P_2 between the two leaflets. LUVs C were prepared in the same way starting from 565 μg of DOPC. The hydrodynamic diameters of the LUVs were determined by dynamic light scattering using a DynaPro99 instrument (Wyatt Technology, formerly Protein Solutions) (39).

Preparation of bovine brain extract

Bovine brain tissue was collected from a nearby slaughterhouse (Bringhurst Meats, Berlin, NJ) and snap-frozen in liquid nitrogen for future use. The brain extract was prepared according to published methods (40). In brief, a piece of flash-frozen bovine brain (10 g) was homogenized on ice with a mortar and pestle in the presence of cOmplete protease inhibitor mixture (Roche Applied Science, Mannheim, Germany) in a 20-ml breaking buffer containing 25 mM Tris, pH 8.0, 500 mM KCl, 250 mM sucrose, 2 mM EGTA, 1 mM DTT. The cell extract was further homogenized with a Dounce homogenizer (Kontes Co., Vineland, NJ) and centrifuged at 160,000 × g for 2 h at 4 °C using a Beckman OptimaTM LE-80K ultracentrifuge and a Ti 70.1 rotor to remove any insoluble debris. The cell extract was desalted on HiTrap Desalting Column (GE Healthcare) at 4 °C into a cytosolic buffer containing 25 mM HEPES, 120 mM potas-

sium glutamate, 20 mM KCl, 2.5 mM $MgCl_2$, and 5 mM EGTA, pH 7.4.

Preparation of neutrophil extract

Supernatant from lysed neutrophils was prepared as described previously (41, 42). Briefly, neutrophils isolated from human blood were resuspended at $\sim 3 \times 10^8$ cells/ml in intracellular physiological buffer (135 mM KCl, 10 mM NaCl, 2 mM $MgCl_2$, 2 mM EGTA, 10 mM HEPES, pH 7.1) containing protease inhibitors (1 μg/ml leupeptin, 1 μg/ml benzamidine, 10 μg/ml aprotinin, 10 μg/ml N^{α}-*p*-tosyl-L-arginine methyl ester). Then, cells were lysed by sonication (three times 2-s pulse on setting 40 of Dynatech Sonic Dismembrator 150; Dynatech Laboratories, Inc.). To obtain supernatant, the neutrophils' lysed suspension was subjected to centrifugation (first, 14,000 rpm ($\sim 1.5 \times 10^5$ g) for 5 min; second, 80,000 rpm for 20 min ($\sim 5.6 \times 10^6$ g). The protein concentration was assessed using a total protein kit (Micro Lowry TP0300, Sigma) and was adjusted to 3 mg/ml. The PI(4,5)P_2 concentration in obtained supernatant was 4.15 pmol/μl as assessed by a PI(4,5)P_2 mass ELISA kit (K-4500, Echelon).

Actin assembly on supported lipid monolayers

Thawed cell extract was supplemented with 1 mM ATP and 20 μM GTPγS before use. Freshly prepared supported lipid monolayer was retrieved from PBS solution. The solution remaining on the coverslip was carefully removed by tissue paper from the side followed by blow-drying briefly to remove tiny droplets that remained attached before applying the cell extract. A cell extract of 50 μl was applied on top of the supported lipid monolayer and incubated on a pre-warmed heating metal block at 37 °C for the indicated periods of time. The samples were fixed by the gentle addition of 50 μl of 1.5% glutaraldehyde solution into the cell extract to avoid actin filament detachment and incubated at room temperature for 40 min. The samples were rinsed with a 10 mM HEPES buffer at pH 7.4 and stained with Alexa Fluor 633-phalloidin (Invitrogen) with a 1:500 or 1:1000 dilution for 30 min. The samples were gently rinsed three times to avoid actin filament detachment, air-dried, and kept away from light for imaging studies. For image analysis, fluorescent micrographs were segmented based on the lipid phases using ImageJ. Average phalloidin intensity within L_o and L_d phases was quantified by randomly selecting fields of view from multiple samples.

EM of supported lipid monolayers

Air-dried supported lipid monolayer samples, with or without assembled actin, were rotary coated with an ~1-nm layer of platinum at a 20° angle and an ~5-nm layer of carbon at an 80° angle using Auto306 vacuum evaporator (Edwards, UK). The coated sample was floated on a diluted hydrofluoric acid solution to separate replica from the coverslip and transferred onto Formvar-coated EM grids. Samples were analyzed using a JEM-1011 transmission electron microscope (JEOL USA, Peabody, MA) at an accelerating voltage of 100 kV. Images were captured by an ORIUS 832.10W CCD camera from samples that were presented in inverse contrast (Gatan, Warrendale, PA).

Actin polymerization assay with LUVs

To induce actin polymerization, a concentrated solution of KCl and $MgCl_2$ was added to G-actin containing ~50% of pyrenyl-actin to obtain 150 mM KCl and 2 mM $MgCl_2$ final concentration. LUVs (0–30 μl) and human neutrophil extract (0–5 μl) were sequentially added. The sample was then topped up to 300 μl with water so that the final G-actin concentration reached 1.7–2 μM, whereas the G-actin concentration in the neutrophil extract was estimated to be around 12 μM. Changes of pyrene fluorescence were monitored for 3–30 min (λ_{ex} 365 nm and λ_{em} 386 nm) using an SL-50B spectrofluorimeter (PerkinElmer Life Sciences). Actin polymerization rate was calculated from the initial slope of the fluorescence increase in the first 30 s. To determine whether PI(4,5)P_2-promoted actin polymerization is mediated by formins or Arp2/3 complex, SMIFH2 (Sigma, S4826) or CK-666 (Sigma, SML0006) was added to the reaction from stock solutions in DMSO. For negative staining EM, a mixture containing G-actin, neutrophil extract, and/or LUVs was loaded onto a carbon-coated EM grid and following incubation for 1–5 min was stained with aqueous 1% uranyl acetate for 1 min before draining and drying. For S1 labeling, after incubation of samples on grids, the grid was passed through 1 drop of S1 (0.25 mg/ml in actin polymerization buffer without ATP), incubated with the second drop of S1 for 5 min, and stained with 1% uranyl acetate.

Actin assembly on plasma membrane sheets

The plasma membrane sheets for actin assembly were prepared based on a published protocol (40). Briefly, plasma membranes of PtK2 cells stably expressing membrane-targeted GFP (GFP-*CAAX*) (gift of Dr. W. Guo, University of Pennsylvania) were isolated by sonication-mediated unroofing. The membrane sheets were incubated at 37 °C with bovine brain extracts supplemented with 0.2 μM rhodamine-actin, 1.5 mM ATP, and 150 μM GTPγS and, optionally, with various pharmacological inhibitors, such as SMIFH2, CK-666, 2 mM neomycin (Sigma, N1876), or MβCD (Sigma, 332615). The samples then were fixed with 0.2% glutaraldehyde in 0.1 M sodium cacodylate, pH 7.3, for 20 min at room temperature. After washing three times with PBS, they were quenched by incubation with $NaBH_4$ (three times for 15 min total), blocked for 30 min with 10% normal goat serum diluted by 0.3 M glycine in PBS, and stained for 1 h with mouse monoclonal IgM antibody to PIP_2 (Abcam, clone 2C11; ab11039) at a 1:60 dilution for fluorescence microscopy or a 1:20 dilution for EM, then with goat anti-mouse IgM CFL-647–conjugated secondary antibody (Santa Cruz Biotechnology, SC-395787, 1:150) for fluorescence microscopy or 18-nm colloidal gold-conjugated secondary antibody (EM Sciences, 25149; 1:10) for EM. To evaluate efficiency of cholesterol depletion from plasma membrane sheets after incubation with MβCD, the sheets were fixed for 20 min with 4% formaldehyde in PBS, quenched with 0.3 M glycine for 10 min, and with 50 μg/ml filipin III (F4767, Sigma) in PBS containing 0.2% saponin and 0.1% BSA for 1 h at room temperature. Samples were washed three times with PBS, mounted into Prolong Gold antifade mountant (P36930, ThermoFisher Scientific), and imaged. Fluorescence imaging was performed using an Eclipse TiE

inverted microscope (Nikon) equipped with a CSUX1 spinning disk (Yokogawa Electric Corp.). For filipin imaging, 405-nm laser and ET455/50M DAPI-ET emission filter was used. EM images were obtained using a JEM 1011 transmission electron microscope (JEOL) operated at 100 kV with an ORIUS 832.10W charge-coupled device camera (Gatan) and presented in inverted contrast.

For quantification of rhodamine-actin incorporation, PI(4,5)P_2 immunofluorescence, and filipin staining, plasma membrane sheets were identified based on GFP-*CAAX* fluorescence, and the mean fluorescence intensities of actin, anti-PI(4,5)P_2, or filipin within the regions of interest chosen away from the membrane sheet margins were measured using ImageJ (FIJI, National Institutes of Health). For quantification of PI(4,5)P_2 immunogold clustering in platinum replica EM images, a number of gold particles per cluster was counted. Gold particles were considered to belong to the same cluster if they were separated by less than twice the diameter of gold particles (36 nm). Statistical significance was determined by Tukey-Kramer multiple comparisons test after evaluating data distribution normality by Kolmogorov-Smirnov normality test using Instat software (GraphPad Software).

Computational methods

Homology modeling of mDia2

Previous co-sedimentation assays conducted on mDia1 demonstrated that peptides spanning basic acid clusters (amino acids 12–21) within the basic domain of mDia1 (amino acids 1–60) are sufficient to bind PI(4,5)P_2 (27). The basic amino acid cluster in mDia1 shares 90% homology with the basic amino acid cluster in mDia2 (amino acids 25–40 with sequence RGCRESKMPRRKGPQH). We created models of this domain (amino acids 25–40) of mDia2. Molecular models of mDia2 were constructed using both the *ab initio* and homology modeling methods Robetta (43) and Modeler (44), respectively, and the highest quality structures yielded from the methods were selected.

To create homology models of the basic mDia2 (amino acids 25–40), the X-ray structure of the human Cdc37 N-terminal domain (Protein Data Bank code 2NCA, amino acids 54–62) was used as a template. The sequences of human Cdc37 N-terminal and human mDia2 were obtained from Uniprot (accessions codes Q16543 and Q9NSV4, respectively). The Clustal Omega (45) program was used to align sequences of the human CDC37 N-terminal domain with the sequence of the human mDia2 indicating the sequences shared 66% identity. This alignment was then used to construct 10 molecular models using Modeler (44). In Robetta (43), the sequence of the basic peptide region was input to the web server, and the resulting structures were analyzed. The top Modeler (44) and Robetta (43) models were selected based on the discrete optimized protein energy score and then relaxed using all-atom molecular dynamics simulations using the molecular dynamics package GROMACS (46), and the CHARMM force field (47). The qualities of the minimized and simulated models were assessed through PROCHECK (48) and SWISS MODEL SERVER (49). PyMOL (50) and Visual Molecular Dynamics (VMD) (51) were used to analyze and visualize the resulting structures. The highest quality selected model based on the assessment methods was selected for the simulations of mDia2 on bilayers.

Table 1
Bilayer compositions utilized in the molecular modeling.

Bilayer	Leaflet	PI(4,5)$P_{2\%}$	DOPE%	DOPS%	POPC%	CHOL%
10% PIP2	Inner	10	50	20	0	20
	Outer	-	-	-	80	20
20% PIP2	Inner	20	40	20	0	20
	Outer	-	-	-	80	20
30% PIP2	Inner	30	30	20	0	20
	Outer	-	-	-	80	20
w/o CHOL	Inner	22	55	23	0	0
	Outer	-	-	-	100	0

Bilayer construction and protein adhesion

To decipher the effect of cholesterol and the importance of PI(4,5)P_2 concentration in PI(4,5)P_2–protein–bilayer interactions, bilayers containing varying concentrations of PI(4,5)P_2 and cholesterol were constructed. We constructed six bilayers containing 10, 20, and 30% PI(4,5)P_2 concentrations and two bilayers containing no cholesterol. Table 1 lists the bilayer composition of the described bilayers. The inner leaflet contained PI(4,5)P_2, DOPE, DOPS, and CHOL, and the outer leaflet contained POPC and CHOL (Fig. 8). DOPE concentrations were adjusted to account for area change when varying the PI(4,5)P_2 and CHOL concentrations. The resulting areas of the bilayers were ~62 nm^2. The simulations were solvated with ~4459 water molecules and neutralized with 239 Na^+ and 71 Cl^- ions. An energy minimization of the solvated bilayer and neutralized structures was performed to correct the inappropriate geometry.

Molecular dynamics of mDia2 on PI(4,5)P_2-containing asymmetric bilayers

In the past, molecular dynamics simulations have revealed unique atomistic resolution characteristics important in understanding protein–membrane interactions and dynamics (52). To decipher the effect and the importance of PI(4,5)P_2 concentration, we performed six all-atom simulations of mDia2 adhered to the bilayers containing varying concentrations of PI(4,5)P_2 listed in Table 1. Then to understand the role of cholesterol, we carried out two simulations mDia2 adhered to the bilayers containing no CHOL.

All simulations were performed using GROMACS version 5.1.2 Charmm36 force field for all standard protein and lipids parameters (53). Long-range interactions were considered through the particle-mesh-Ewald method. mDia2 was placed on a previously equilibrated bilayer containing water molecules and counter sodium and chloride ions and ~252 lipids. mDia2 was adhered to at least one PI(4,5)P_2 molecule at the center of the bilayer with a distance of 3 Å. The simulations were solvated with ~4459 water molecules. The Linear Constraint Solver (LINCS) algorithm was used to constrain bond lengths. Each system was simulated for 150 ns in the semi-isotropic NPT ensemble, with constant particle number *N*, normal pressure of 1 atm, and constant temperature of 300 K. A time step of 1 fs was used in all simulations. The resulting simulations were viewed and analyzed using VMD and in-house analysis codes

based on software shared on line at http://biophyscode.github.io.[4] A typical dynamics run required 432 h of computing time on a single 16-core CPU.

Continuum spatial model of actin filament formation on the membrane

The spatial model for actin nucleation consists of the following: (i) a patch of the cell membrane of 500 × 500-nm dimension simulated using the dynamically triangulated Monte Carlo method (54); and (ii) actin monomers that can polymerize at the nucleation sites on the membrane surface. A snapshot of the simulation is shown in Fig. 11*A*. The membrane is placed in a periodic box, and the direction perpendicular to the membrane plane is taken to be the z direction. Actin nucleation sites are allocated at a random position on the membrane. Monomers of actin are taken to be coarse-grained beads and are allowed to reside and diffuse in the box, on one side membrane, with periodic boundary conditions in the x and y directions. New actin filaments are nucleated from actin nucleation complexes on the membrane with the filament barbed end toward the membrane. After nucleation, filaments polymerize at the barbed end and depolymerize at the pointed end. Filament growth is modeled as diffusion-limited aggregation and de-polymerization as a stochastic event for each filament (55). The ratio of polymerization to depolymerization is set to be comparable with experimental values (8 μM). Actin filaments are treated as semi-flexible filaments with persistence length (l_p) = 10 μm. The bound monomers in a filament interact with the connected neighbors via a spring potential $E_{\text{spring}} = k_{\text{spring}}(r - a)^2/2$ and an angle potential $E_{\text{bend}} = k_{\text{bend}}(1 - \cos\theta)/2$. Here a, the diameter of the monomers, is taken to be 7 nm, comparable with the diameter of actin filaments. We take $k_{\text{bend}} = k_B T l_p/a$ and $k_{\text{bend}} = k_{\text{spring}}$. The concentration of actin monomers is taken to be 100 μM.

Author contributions—R. Bucki, Y.-H. W., C. Y., S. K. K., R. Bradley, T. S., R. R., and P. A. J. conceptualization; R. Bucki, T. S., R. R., and P. A. J. funding acquisition; R. Bucki, Y.-H. W., C. Y., S. K. K., O. F., R. Bradley, K. P., T. S., R. R., and P. A. J. writing-original draft; Y.-H. W., C. Y., S. K. K., and P. A. J. investigation; Y.-H. W., C. Y., O. F., R. Bradley, K. P., T. S., R. R., and P. A. J. methodology; C. Y., T. S., and R. R. visualization; S. K. K., R. Bradley, R. R., and P. A. J. formal analysis; K. P. data curation; T. S. and P. A. J. supervision; T. S. and P. A. J. project administration; T. S. and P. A. J. writing-review and editing; R. R. and P. A. J. validation; P. A. J. resources.

Acknowledgments—We thank Dr. Michael Marks and Yueyao Zhu for help with filipin staining and imaging.

References

1. Lassing, I., and Lindberg, U. (1985) Specific interaction between phosphatidylinositol 4,5-bisphosphate and profilactin. *Nature* **314,** 472–474 CrossRef Medline
2. Yin, H. L., and Janmey, P. A. (2003) Phosphoinositide regulation of the actin cytoskeleton. *Annu. Rev. Physiol.* **65,** 761–789 CrossRef Medline
3. Shibasaki, Y., Ishihara, H., Kizuki, N., Asano, T., Oka, Y., and Yazaki, Y. (1997) Massive actin polymerization induced by phosphatidylinositol-4-phosphate 5-kinase *in vivo*. *J. Biol. Chem.* **272,** 7578–7581 CrossRef Medline
4. Yamamoto, M., Hilgemann, D. H., Feng, S., Bito, H., Ishihara, H., Shibasaki, Y., and Yin, H. L. (2001) Phosphatidylinositol 4,5-bisphosphate induces actin stress-fiber formation and inhibits membrane ruffling in cv1 cells. *J. Cell Biol.* **152,** 867–876 CrossRef Medline
5. Sakisaka, T., Itoh, T., Miura, K., and Takenawa, T. (1997) Phosphatidylinositol 4,5-bisphosphate phosphatase regulates the rearrangement of actin filaments. *Mol. Cell. Biol.* **17,** 3841–3849 CrossRef Medline
6. Varnai, P., Thyagarajan, B., Rohacs, T., and Balla, T. (2006) Rapidly inducible changes in phosphatidylinositol 4,5-bisphosphate levels influence multiple regulatory functions of the lipid in intact living cells. *J. Cell Biol.* **175,** 377–382 CrossRef Medline
7. Ma, L., Cantley, L. C., Janmey, P. A., and Kirschner, M. W. (1998) Corequirement of specific phosphoinositides and small GTP-binding protein cdc42 in inducing actin assembly in *Xenopus* egg extracts. *J. Cell Biol.* **140,** 1125–1136 CrossRef Medline
8. Lee, K., Gallop, J. L., Rambani, K., and Kirschner, M. W. (2010) Self-assembly of filopodia-like structures on supported lipid bilayers. *Science* **329,** 1341–1345 CrossRef Medline
9. Kwik, J., Boyle, S., Fooksman, D., Margolis, L., Sheetz, M. P., and Edidin, M. (2003) Membrane cholesterol, lateral mobility, and the phosphatidylinositol 4,5-bisphosphate-dependent organization of cell actin. *Proc. Natl. Acad. Sci. U.S.A.* **100,** 13964–13969 CrossRef Medline
10. Jungmichel, S., Sylvestersen, K. B., Choudhary, C., Nguyen, S., Mann, M., and Nielsen, M. L. (2014) Specificity and commonality of the phosphoinositide-binding proteome analyzed by quantitative mass spectrometry. *Cell Rep.* **6,** 578–591 CrossRef Medline
11. Janmey, P. A., Bucki, R., and Radhakrishnan, R. (2018) Regulation of actin assembly by PI(4,5)P2 and other inositol phospholipids: an update on possible mechanisms. *Biochem. Biophys. Res. Commun.* **506,** 307–314 CrossRef Medline
12. Golebiewska, U., Nyako, M., Woturski, W., Zaitseva, I., and McLaughlin, S. (2008) Diffusion coefficient of fluorescent phosphatidylinositol 4,5-bisphosphate in the plasma membrane of cells. *Mol. Biol. Cell* **19,** 1663–1669 CrossRef Medline
13. Wang, Y. H., Bucki, R., and Janmey, P. A. (2016) Cholesterol-dependent phase-demixing in lipid bilayers as a switch for the activity of the phosphoinositide-binding cytoskeletal protein gelsolin. *Biochemistry* **55,** 3361–3369 CrossRef Medline
14. Honigmann, A., van den Bogaart, G., Iraheta, E., Risselada, H. J., Milovanovic, D., Mueller, V., Müllar, S., Diederichsen, U., Fasshauer, D., Grubmüller, H., Hell, S. W., Eggeling, C., Kühnel, K., and Jahn, R. (2013) Phosphatidylinositol 4,5-bisphosphate clusters act as molecular beacons for vesicle recruitment. *Nat. Struct. Mol. Biol.* **20,** 679–686 CrossRef Medline
15. van den Bogaart, G., Meyenberg, K., Risselada, H. J., Amin, H., Willig, K. I., Hubrich, B. E., Dier, M., Hell, S. W., Grubmüller, H., Diederichsen, U., and Jahn, R. (2011) Membrane protein sequestering by ionic protein-lipid interactions. *Nature* **479,** 552–555 CrossRef Medline
16. Wang, J., and Richards, D. A. (2012) Segregation of PIP2 and PIP3 into distinct nanoscale regions within the plasma membrane. *Biol. Open* **1,** 857–862 CrossRef Medline
17. Chierico, L., Joseph, A. S., Lewis, A. L., and Battaglia, G. (2014) Live cell imaging of membrane/cytoskeleton interactions and membrane topology. *Sci. Rep.* **4,** 6056 Medline
18. Kang, J. K., Kim, O. H., Hur, J., Yu, S. H., Lamichhane, S., Lee, J. W., Ojha, U., Hong, J. H., Lee, C. S., Cha, J. Y., Lee, Y. J., Im, S. S., Park, Y. J., Choi, C. S., Lee, D. H., *et al.* (2017) Increased intracellular Ca^{2+} concentrations prevent membrane localization of pH domains through the formation of Ca^{2+}-phosphoinositides. *Proc. Natl. Acad. Sci. U.S.A.* **114,** 11926–11931 CrossRef Medline
19. Rizvi, S. A., Neidt, E. M., Cui, J., Feiger, Z., Skau, C. T., Gardel, M. L., Kozmin, S. A., and Kovar, D. R. (2009) Identification and characterization of a small molecule inhibitor of formin-mediated actin assembly. *Chem. Biol.* **16,** 1158–1168 CrossRef Medline

[4] Please note that the JBC is not responsible for the long-term archiving and maintenance of this site or any other third party hosted site.

20. Nolen, B. J., Tomasevic, N., Russell, A., Pierce, D. W., Jia, Z., McCormick, C. D., Hartman, J., Sakowicz, R., and Pollard, T. D. (2009) Characterization of two classes of small molecule inhibitors of arp2/3 complex. *Nature* **460,** 1031–1034 CrossRef Medline
21. Lassing, I., and Lindberg, U. (1988) Evidence that the phosphatidylinositol cycle is linked to cell motility. *Exp. Cell Res.* **174,** 1–15 CrossRef Medline
22. Lewis, A. E., Sommer, L., Arntzen, M. O., Strahm, Y., Morrice, N. A., Divecha, N., and D'Santos, C. S. (2011) Identification of nuclear phosphatidylinositol 4,5-bisphosphate-interacting proteins by neomycin extraction. *Mol. Cell. Proteomics* **10,** M110.003376 CrossRef Medline
23. Mahammad, S., and Parmryd, I. (2015) Cholesterol depletion using methyl-β-cyclodextrin. Methods Mol. Biol. **1232,** 91–102 CrossRef Medline
24. Collins, A., Warrington, A., Taylor, K. A., and Svitkina, T. (2011) Structural organization of the actin cytoskeleton at sites of clathrin-mediated endocytosis. *Curr. Biol.* **21,** 1167–1175 CrossRef Medline
25. Tomasevic, N., Jia, Z., Russell, A., Fujii, T., Hartman, J. J., Clancy, S., Wang, M., Beraud, C., Wood, K. W., and Sakowicz, R. (2007) Differential regulation of WASP and N-WASP by Cdc42, Rac1, Nck, and PI(4,5)P2. *Biochemistry* **46,** 3494–3502 CrossRef Medline
26. Suetsugu, S., Miki, H., Yamaguchi, H., Obinata, T., and Takenawa, T. (2001) Enhancement of branching efficiency by the actin filament-binding activity of N-WASP/WAVE2. *J. Cell Sci.* **114,** 4533–4542 Medline
27. Ramalingam, N., Zhao, H. X., Breitsprecher, D., Lappalainen, P., Faix, J., and Schleicher, M. (2010) Phospholipids regulate localization and activity of mdia1 formin. *Eur. J. Cell Biol.* **89,** 723–732 CrossRef Medline
28. Gorelik, R., Yang, C., Kameswaran, V., Dominguez, R., and Svitkina, T. (2011) Mechanisms of plasma membrane targeting of formin mdia2 through its amino-terminal domains. *Mol. Biol. Cell* **22,** 189–201 CrossRef Medline
29. Veatch, S. L., and Keller, S. L. (2005) Miscibility phase diagrams of giant vesicles containing sphingomyelin. *Phys. Rev. Lett.* **94,** 148101 CrossRef Medline
30. Veatch, S. L., and Keller, S. L. (2003) Separation of liquid phases in giant vesicles of ternary mixtures of phospholipids and cholesterol. *Biophys. J.* **85,** 3074–3083 CrossRef Medline
31. Rusinova, R., Hobart, E. A., Koeppe, R. E., 2nd., and Andersen, O. S. (2013) Phosphoinositides alter lipid bilayer properties. *J. Gen. Physiol.* **141,** 673–690 CrossRef Medline
32. Levental, I., and Janmey, P. A., and Cēbers, A. (2008) Electrostatic contribution to the surface pressure of charged monolayers containing polyphosphoinositides. *Biophys. J.* **95,** 1199–1205 CrossRef Medline
33. Wang, Y. H., Collins, A., Guo, L., Smith-Dupont, K. B., Gai, F., Svitkina, T., and Janmey, P. A. (2012) Divalent cation-induced cluster formation by polyphosphoinositides in model membranes. *J. Am. Chem. Soc.* **134,** 3387–3395 CrossRef Medline
34. Bilkova, E., Pleskot, R., Rissanen, S., Sun, S., Czogalla, A., Cwiklik, L., Róg, T., Vattulainen, I., Cremer, P. S., Jungwirth, P., and Coskun, Ü. (2017) Calcium directly regulates phosphatidylinositol 4,5-bisphosphate headgroup conformation and recognition. *J. Am. Chem. Soc.* **139,** 4019–4024 CrossRef Medline
35. Wang, Y. H., Slochower, D. R., and Janmey, P. A. (2014) Counterion-mediated cluster formation by polyphosphoinositides. *Chem. Phys. Lipids* **182,** 38–51 CrossRef Medline
36. Ridley, A. J. (2015) Rho GTPase signalling in cell migration. *Curr. Opin. Cell Biol.* **36,** 103–112 CrossRef Medline
37. Senju, Y., Kalimeri, M., Koskela, E. V., Somerharju, P., Zhao, H., Vattulainen, I., and Lappalainen, P. (2017) Mechanistic principles underlying regulation of the actin cytoskeleton by phosphoinositides. *Proc. Natl. Acad. Sci. U.S.A.* **114,** E8977–E8986 CrossRef Medline
38. Alwarawrah, M., and Wereszczynski, J. (2017) Investigation of the effect of bilayer composition on PKCα-C2 domain docking using molecular dynamics simulations. *J. Phys. Chem. B* **121,** 78–88 CrossRef Medline
39. Bucki, R., Pastore, J. J., Randhawa, P., Vegners, R., Weiner, D. J., and Janmey, P. A. (2004) Antibacterial activities of rhodamine B-conjugated gelsolin-derived peptides compared with those of the antimicrobial peptides cathelicidin LL37, magainin II, and melittin. *Antimicrob. Agents Chemother.* **48,** 1526–1533 CrossRef Medline
40. Wu, M., Huang, B., Graham, M., Raimondi, A., Heuser, J. E., Zhuang, X., and De Camilli, P. (2010) Coupling between clathrin-dependent endocytic budding and F-BAR-dependent tubulation in a cell-free system. *Nat. Cell Biol.* **12,** 902–908 CrossRef Medline
41. Huang, M., Pring, M., Yang, C., Taoka, M., and Zigmond, S. H. (2005) Presence of a novel inhibitor of capping protein in neutrophil extract. *Cell Motil. Cytoskeleton* **62,** 232–243 CrossRef Medline
42. Zigmond, S. H., Joyce, M., Yang, C., Brown, K., Huang, M., and Pring, M. (1998) Mechanism of Cdc42-induced actin polymerization in neutrophil extracts. *J. Cell Biol.* **142,** 1001–1012 CrossRef Medline
43. Kim, D. E., Chivian, D., and Baker, D. (2004) Protein structure prediction and analysis using the Robetta server. *Nucleic Acids Res.* **32,** W526–W531 CrossRef Medline
44. Eswar, N., Webb, B., Marti-Renom, M. A., Madhusudhan, M. S., Eramian, D., Shen, M. Y., Pieper, U., and Sali, A. (2006) Comparative protein structure modeling using Modeller. *Curr. Protoc.* Bioinformatics 2006 Chapter 5, Unit 5.6 CrossRef Medline
45. Sievers, F., and Higgins, D. G. (2018) Clustal Omega for making accurate alignments of many protein sequences. *Protein Sci.* **27,** 135–145 CrossRef Medline
46. Van Der Spoel, D., Lindahl, E., Hess, B., Groenhof, G., Mark, A. E., and Berendsen, H. J. (2005) Gromacs: fast, flexible, and free. *J. Comput. Chem.* **26,** 1701–1718 CrossRef Medline
47. Stocker, U., and van Gunsteren, W. F. (2000) Molecular dynamics simulation of hen egg white lysozyme: a test of the GROMOS96 force field against nuclear magnetic resonance data. *Proteins* **40,** 145–153 CrossRef Medline
48. Laskowski, R. A., Rullmannn, J. A., MacArthur, M. W., Kaptein, R., and Thornton, J. M. (1996) AQUA and PROCHECK-NMR: programs for checking the quality of protein structures solved by NMR. *J. Biomol. NMR* **8,** 477–486 Medline
49. Biasini, M., Bienert, S., Waterhouse, A., Arnold, K., Studer, G., Schmidt, T., Kiefer, F., Gallo Cassarino, T., Bertoni, M., Bordoli, L., and Schwede, T. (2014) Swiss-Model: modelling protein tertiary and quaternary structure using evolutionary information. *Nucleic Acids Res.* **42,** W252–W258 CrossRef Medline
50. DeLano, W. L. (2002) *The PyMOL Molecular Graphics System.* DeLano Scientific LLC, San Carlos, CA
51. Humphrey, W., Dalke, A., and Schulten, K. (1996) VMD: visual molecular dynamics. *J. Mol. Graph.* **14,** 33–38, 27–8 CrossRef Medline
52. Bradley, R. P., and Radhakrishnan, R. (2016) Curvature-undulation coupling as a basis for curvature sensing and generation in bilayer membranes. *Proc. Natl. Acad. Sci. U.S.A.* **113,** E5117–E5124 CrossRef Medline
53. Lee, S., Tran, A., Allsopp, M., Lim, J. B., Hénin, J., and Klauda, J. B. (2014) Charmm36 united atom chain model for lipids and surfactants. *J. Phys. Chem. B* **118,** 547–556 CrossRef Medline
54. Ramakrishnan, N., Sunil Kumar, P. B., and Radhakrishnan, R. (2014) Mesoscale computational studies of membrane bilayer remodeling by curvature-inducing proteins. *Phys. Rep.* **543,** 1–60 CrossRef Medline
55. Dogterom, M., and Leibler, S. (1993) Physical aspects of the growth and regulation of microtubule structures. *Phys. Rev. Lett.* **70,** 1347–1350 CrossRef Medline